INSPECTION OF EXCITED STATE PROPERTIES IN DEFECTED CARBON NANOTUBES FROM MULTIPLE EXCITON GENERATION TO DEFECT-DEFECT INTERACTIONS

A Thesis
Submitted to the Graduate Faculty
of the
North Dakota State University
of Agriculture and Applied Science

By

Braden Michael Weight

In Partial Fulfillment of the Requirements
for the Degree of
MASTER OF SCIENCE

Major Department:
Physics

April 2020

Fargo, North Dakota

NORTH DAKOTA STATE UNIVERSITY

Graduate School

Title

INSPECTION OF EXCITED STATE PROPERTIES IN DEFECTED CARBON NANOTUBES FROM MULTIPLE EXCITON GENERATION TO DEFECT-DEFECT INTERACTIONS

By

Braden Michael Weight

The supervisory committee certifies that this thesis complies with North Dakota State University's regulations and meets the accepted standards for the degree of

MASTER OF SCIENCE

SUPERVISORY COMMITTEE:

Prof. Andrei Kryjevski

Chair

Prof. Dmitri Kilin

Prof. Alan Denton

Prof. Erik Hobbie

Approved:

April 24, 2020

Date

Sylvio May

Department Chair

ABSTRACT

Covalent SP^3-hybridization defects in single-walled carbon nanotubes (CNTs) have been prevalent in recent experimental and theoretical studies for their interesting photophysical properties. These systems are able to act as excellent sources of single, infrared photons, even at room temperature, making them marketable for applications to sensing, telecommunications, and quantum information. This work was motivated by recent experimental studies on controllable defect placement and concentration as well as investigating carrier multiplication (CM) using DFT-based many-body perturbation theory (MBPT) methods to describe excitonic relaxation processes. We find that pristine CNTs do not yield appreciable MEG at the minimum threshold of twice the optical gap $2E_g$, but covalent functionalization allows for improved MEG at the threshold. Finally, we see that defect-defect interactions within CNT systems can be modeled simply as HJ-aggregates in an effective Hamiltonian model, which is shown to be valid for certain, highly-redshifted defect configurations at low defect-defect separation lengths.

ACKNOWLEDGEMENTS

I acknowledge helpful discussions with Andrei Kryjevski, Brendan Gifford, Svetlana Kilina, Dmitri Kilin, Sergei Tretiak, and Nathan Walker. In addition, all the computations were performed using NDSU's Center for Computationally Assisted Science and Technology (CCAST).

TABLE OF CONTENTS

ABSTRACT iii

ACKNOWLEDGEMENTS iv

LIST OF TABLES vi

LIST OF FIGURES vii

LIST OF APPENDIX FIGURES x

1. ENHANCED OPTICAL PROPERTIES OF SINGLE-WALLED CARBON NANOTUBES VIA SP^3-HYBRIDIZATION DEFECTS FROM MANY-BODY PERTURBATION THEORY BASED ON DENSITY FUNCTIONAL THEORY CALCULATIONS 1

   1.1. Introduction 1

   1.2. Model and Methods 2

   1.3. Results and Discussion 6

   1.4. Conclusion 12

2. INTERACTING PAIRS OF SURFACE DEFECTS ON CARBON NANOTUBES 14

   2.1. Introduction 14

   2.2. Methodology 17

   2.3. Results and Discussion 20

      2.3.1. Ground State Properties 20

      2.3.2. Excited State Properties 22

   2.4. Conclusions 29

REFERENCES 31

APPENDIX. SUPPLEMENTAL INFORMATION 41

LIST OF TABLES

Table Page

1.1. Geometry details of initial pristine systems used as input to geometry optimization. . . 2

1.2. E_{HL} and E_{11} values for all pristine CNTs compared to experimental data. All values are in eV. 7

1.3. Various energy values for defects CNTs, where $\Delta E_{11} = E_{11}^{Pristine} - E_{11}^{*}$. All data is given in eV. 8

LIST OF FIGURES

Figure Page

1.1. In our approximation, we take the HSE06 functional to give semi-accurate single-particle orbitals as a substitution for a full GW quasi-particle calculation. In turn, this redshifts our single-particle energies in comparison and is the main drawback of our methods. However, this redshift is shown later to be systematic and gives high precision energies for all systems (i.e., the standard deviation is small when comparing the redshift across all systems). 3

1.2. Absorption rates for various pristine (a) and functionalized (b,c) CNTs. Vertical dashed lines correspond to experimental results for low-energy absorption at the E_{11} band. Note redshift dependence is dictated by both chirality and configuration of defects, therefore, all excited state properties will be governed by these same parameters. 6

1.3. Exciton (blue) and biexciton (green) DOS for various pristine and functionalized CNTs. The functionalized geometries are arranged such that the middle row produces less redshift than the bottom row. At $2E_g$, the biexciton DOS of the most redshifted defect configurations is equal to or higher than exciton DOS, indicating optimal conditions for minimum-threshold QE. Note the units of DOS are inverse energy and that thermally broadened δ-functions (Gaussian width = 25 meV) were used. 9

1.4. Exciton-to-biexciton rates for various pristine (a) and functionalized (b,c) CNTs. Keeping in mind, these rates are only part of the picture without considering competition with phonons, all pristine CNTs except (6,5) have negligible biexciton formation rates until about 2.4 E_g. Upon functionalization, in three of the four cases, the biexciton formation threshold is lowered to its minimum of $2E_g$. In all cases, the overall rates are increased upon functionalization due to the increased DOS. (10,5) 2Cl O+ produced a reduction but only from 2.5 E_g to 2.3 E_g. This may be a consequence of both diameter and configuration, as the O+ in (10,5) produces minimal redshift from the already low-energy pristine exciton. It is hypothesized that the least redshifted configuration is the least effective configuration to reduce the MEG threshold from pristine. 11

1.5. Internal quantum efficiency for a subset of systems studied in this work: Pristine (10,5), (6,5), and (9,1) as well as Cl/Cl functionalized (10,5) in O+ and P+ configurations. Panels (a,c) are shown as a function of photon energy. Panels (b,d) show the same information but in energy normalized by the optical gap E_g. 12

2.1. Transition state diagram according to general Kasha theory on HJ aggregates. H-aggregates are formed by stacking two "monomers", producing blue shifted transition energies in comparison to the single aggregate, stemming from the fact that parallel transition dipole moments are stacked. J-aggregates are formed similarly by "head-to-tail" orientation instead of stacked, which switches the bright and dark states, producing a red shifted transition, respectively. 16

2.2. Carbon nanotubes (CNTs) carrying two or more covalent defects have strong similarities to interacting molecular aggregates that allow for splitting between excitonic states through dipolar interaction. We see increased tunability by modifying the separation distance between the defects, which allows for increased redshifting beyond the previous limit of diameter and configuration dependent thresholds. 17

2.3. Four types of binding geometries for two pairs of defects, where L = 10 separating carbons. Binding geometries: (a) Axial L 11, (b) Axial 3L 31, (c) Circumferential L 12, and (d) Axial L Circumferential L 12. 18

2.4. Thermodynamic stability of each geometry studied is shown here. (a) Single defect total energies are shown subtracted from the pristine total energy, which we label $\Delta 1$, $\Delta 2$, and $\Delta 3$, respectively. (b) All defect geometries calculated and their respective total energies, again subtracted from the pristine total energy. The dashed lines represent different additive combinations of $\Delta 1$, $\Delta 2$, and $\Delta 3$, which clearly show that the stability of defect pair combinations is simply the addition of the two defect pairs that comprise that combination. This becomes more and more accurate as the interaction (i.e. distance) between the defect pairs becomes weaker and weaker moving from Axial L to 3L. CL represent a circumferential translation of length L, and AL/CL represents an axial translation of length L followed by a circumferential translation of length L. (c) The deviation from this additive hypothesis is plotted. The circumferential configuration shows the most deviation from this trend, showing that some configurations are more stable than others. 21

2.5. Absorption spectrum for four geometries, including both the bright pristine E_{11} transition ($\sim$2.05 eV) and the bright (and dark) defect-associated transitions ($\sim$1.4 – 1.7 eV). Single defect in the type-1 configuration as reference for the J coupling value. With increasing distance L, 2L, to 3L, we see an increase in J-splitting symmetry as well as a decrease in J-splitting magnitude. The splitting becomes more and more symmetric due to the increase in distance, which implies that the wavefunctions of each defect are becoming less overlapped and becoming more and more ideal to the simple Kasha model. In addition, since $J \sim 1/r^3$ in the point-dipole approximation, the magnitude of splitting decreases with increasing defect-defect distance r. Note that the vertical axis scale represents unitless oscillator strength and not absorption, which has arbitrary units. 22

2.6. (a) J-coupling values for same-defect axial geometries (i.e. 11, 22, 33) using Eq. 2.4. (b) J-coupling values for off-diagonal defect axial geometries (i.e. 21, 31, 32) using Eq. 2.2. Dotted lines show power law fits to the data according to (Eq. 2.5), with the power from fitting is shown next to each respective line; AX^n. (c) Deviation from single-defect transition energy of the mean transition energies for same-defect axial geometries. (d) Deviation from single-defect transition energy for each defect in a pair of defects. As the defects approach infinite separation length, each panel should tend to zero for completely independent defects. Panels (a-c) conform to panel (a) legend. Panel (d) conforms to both panel (a) and (d) legends. Note the change in vertical scale of panel (d). 24

2.7. (a) Cartoon of interacting defects along the axial direction, where the transition dipole moments make a J-type aggregate. (b) Similarly to (a), the depth of the well is depicted by the intense exciton localization nature of the 1-type defect in comparison to the 2-type defect, where the 1-type "cannibalizes" the localization of the exciton. (c) Depiction of the circumferential geometry potential energy, effectively forming an H-type aggregate by the stacking of the transition dipole moments. 25

2.8. Spatially-resolved transition density for six different geometries: Axial L 11, 21, 31 and Axial 3L 11, 21, 31 showcasing the various interaction of defects from the perspective of interacting wells. The more red-shifted defects "cannibalize" the nearby density of other defects. 26

2.9. Analogously to Fig. A.11, coupling values for each method of calculation: (I) from oscillator energy splitting and (II) from single-molecule dipoles. For J-type aggregates, we see qualitative agreement between the methods, but the H-type aggregates breakdown in this comparison, as the systems never produce H-type splitting. All defects were of 11 type. 27

LIST OF APPENDIX FIGURES

Figure Page

A.1. Definition of defect orientation. With one attachment placed at R_1, the second attachment can be placed in any of the nearest six carbon atoms: Three ortho and three para to the original location. In this study, we restrict ourselves to the most and least redshifted configurations: P+ and O+, respectively. 41

A.2. Phonon density of states (DOS) for all pristine (a) and chlorine-functionalized (b,c) CNTs. Phonon spectrum was computed using VASP at the PBE level using two-point differences. Due to the more narrow (6,2) CNT, we see larger differences arising from the increased curvature as well as smaller number of defect atoms to total atoms in comparison to (10,5). Note the units of DOS are inverse energy and that thermally broadened δ-functions (Gaussian width = 25 meV) were used. 42

A.3. Definition of defect configuration. One covalently bonded group is fixed at R1, but there are three (i.e., type 1, 2, or 3) non-equivalent ortho positions to place the second covalent attachment (needed for closed shell system). In previous works using the (6,5) CNT, these were labeled as O+, O++, and O- or as L30, L90, and L-30. Here we employ a chirality independent nomenclature to describe the defects by their amount of redshift produced from the pristine E11 band. 42

A.4. Absorption spectrum for four geometries, including both the bright pristine E11 transition (∼2.05 eV) and the bright (and dark) defect-associated transitions (∼1.8 – 1.9 eV). Single defect in the 2-type configuration as reference for the J coupling value. With increasing distance L, 2L, to 3L, we see an increase in J-splitting symmetry as well as a decrease in J-splitting magnitude, except for the smallest distance "Axial L" due to intense wavefunction overlap. The midpoint of the splitting becomes more and more symmetric due to the increase in distance, which implies that the wavefunctions of each defect are becoming less overlapped and becoming more and more ideal to the simple Kasha model. In addition, since $J \sim 1/r^3$, the magnitude of splitting decreases with increasing defect-defect distance r. Note that the vertical axis scale represents unitless oscillator strength and not absorption, which has arbitrary units. 43

A.5. S2: Absorption spectrum for four geometries, including both the bright pristine E11 transition (∼2.05 eV) and the bright (and dark) defect-associated transitions (∼1.85 – 1.95 eV). Single defect in the 3-type configuration as reference for the J coupling value. With increasing distance L, 2L, to 3L, we see an increase in J-splitting symmetry as well as a decrease in J-splitting magnitude. The midpoint of the splitting becomes more and more symmetric due to the increase in distance, which implies that the wavefunctions of each defect are becoming less overlapped and becoming more and more ideal to the simple Kasha model. In addition, since $J \sim 1/r^3$, the magnitude of splitting decreases with increasing defect-defect distance r. Note that the vertical axis scale represents unitless oscillator strength and not absorption, which has arbitrary units. 44

A.6. Absorption spectrum for all six combinations of defect pairs with a separation distance of L. Note that the vertical axis scale represents unitless oscillator strength and not absorption, which has arbitrary units. 45

A.7. Absorption spectrum for all six combinations of defect pairs with a separation distance of 2L. Note that the vertical axis scale represents unitless oscillator strength and not absorption, which has arbitrary units. 46

A.8. Absorption spectrum for all six combinations of defect pairs with a separation distance of 3L. Note that the vertical axis scale represents unitless oscillator strength and not absorption, which has arbitrary units. 47

A.9. Absorption spectrum for all six combinations of defect pairs with a separation distance of 4L. Note that the vertical axis scale represents unitless oscillator strength and not absorption, which has arbitrary units. 48

A.10. Absorption spectra of the model system, comprised of interacting single molecules. Showing the monomer transition (black) for reference, we computed the H-aggregate (red) limit and the J-aggregate (blue) limit to compare the unique qualities of each for use of analysis of the more complicated CNT case. We introduce a model system (see Fig. A.10), comprised of a single molecule (perylene) with a spectrally unique transition near 4.1 eV (as calculated from TD-DFT at the same level of theory as our CNT calculations). Fig. A.10 shows the limiting cases of H- (red) and J- (blue) aggregate geometries that blue-shift and red-shift the bright state, respectively, in comparison to the monomer transition energy (black). A scan over the angle between the transition dipole and the center-to-center vector between the molecules is carried out by starting with a stacked geometry (H-aggregate, $\theta = 90$ and shifting the bottom molecule along the slip plane. 49

A.11. Coulomb coupling values for each method of calculation: (I) from oscillator energy splitting and (II) from single-molecule dipoles, where the latter assumes the form of the coupling, but the former does not. We see qualitative agreement between the two methods, especially for J-type interaction regions. Using Eq. 2.2 and Eq. 2.3 to calculate, separately, the coupling via oscillators and single-monomer transition dipoles, we provide direct comparison between the theory and numerical experiment. Fig. S8a shows the coupling is plotted against the angle of interaction using the center of mass of each molecule as its transition dipole origin. The coupling plotted against the independent variable in the point dipole approximation. The form of this function was explicitly used to acquire the coupling from the dipoles, so this depiction expands on where the method of oscillators deviates from this model. The deviations occur around $\theta = 30$ where we expect the point dipole approximation to become less trustworthy. To minimize the vibrational coupling in this molecular system when stacked, which has been studied in depth by various groups, a slightly larger distance than would appear in experiment was used as the stacking distance to concentrate purely on the long-range Coulomb interactions. In addition, there may be errors stemming from our limited basis and methodology that contribute to these deviations. Even though the shape of the curve is modified through these higher-order effects, the general form of the function with regards to the dipole approximation is recovered and can be used in comparison to the CNT system. 50

A.12. Transition density is shown for the model system in three geometries, the monomer and two dimers that are the limiting cases of the interaction angle θ. We note simply the symmetries for each set of aggregates that exhibit bright transitions and dark transitions. In addition to calculating the Coulomb coupling of these interactions, we may examine these objects from a visual perspective by plotting the transition density for the two excited states in question and examining the unique qualities of each type of aggregate. In Fig. A.12, we show transition density for three systems: (I) monomer, (II) H-type aggregate, and (III) J-type aggregate. For the two aggregates, we also show the two interacting states, $S_{1,2}$, where we know from the effective exciton model, that the lower state should be dark (H-type) for one and bright (J-type) for the other. After examination of the transition density, we find that there are inherent symmetries with respect to the transition states of each molecule in the dimer that will allow or disallow that optical transition, which we will not discuss in depth, as this is already well known. We simply note that one molecule in a dimer will always resemble the single-molecule (monomer) case, and the other molecule is either identical or related to the first by a C2 rotation about the axis perpendicular to the plane of the molecule. When the dimer exhibits the latter property, the state is said to be dark, which physically manifests itself in the fact that the electric transition dipoles are now anti-parallel, since the electron and hole spatial occupations have switched. In the bright case, the transition densities of both molecules are identical to each other and, hence, have parallel dipoles. 51

A.13. Absorption spectrum for all six combinations of defect pairs with circumferential translation, $\theta \sim 90$ Note that the vertical axis scale represents unitless oscillator strength and not absorption, which has arbitrary units. 52

A.14. Absorption spectrum for all six combinations of defect pairs with circumferential translation and axial translation such that $\theta \sim 45$ Note that the vertical axis scale represents unitless oscillator strength and not absorption, which has arbitrary units. 53

A.15. Transition density for various type 11 CNT systems that have been used to sample the angle space of this interaction. One defect was circumferentially translated and then axially translated by various lengths. These densities show various important characteristics from symmetry of each defect to the ordered state along each side of the CNT. 54

A.16. Transition density for various type 11 CNT systems that have been used to sample the angle space of this interaction. One defect was circumferentially translated and then axially translated by various lengths. These densities show various important characteristics from symmetry of each defect to the ordered state along each side of the CNT. 55

A.17. Energies of CNT excited states S_1 and S_2, also plotted with the Coulomb coupling as a function of axial separation. 56

1. ENHANCED OPTICAL PROPERTIES OF SINGLE-WALLED CARBON NANOTUBES VIA SP^3-HYBRIDIZATION DEFECTS FROM MANY-BODY PERTURBATION THEORY BASED ON DENSITY FUNCTIONAL THEORY CALCULATIONS

1.1. Introduction

Carbon nanotubes (CNTs) have an unusually wide array of applications in mechanical engineering as well as in optical and electronic response [1–3]. In this work, we focus on the latter two. Even within these areas, these nanoscopic objects are well-suited for both single-photon emission as well as light-harvesting carrier multiplication (CM), leading to many studies over the last two decades on these topics [4–13]. The methodology for computationally investigating CM to an accurate level has only just begun to reach usable quality, and even now, we can only attain qualitative accuracy. Much of the usual methods for computing carrier multiplication processes have been restricted to density functional theory (DFT) models, where single-particle Kohn-Sham states were used to compute trion rates neglecting excitonic effects [14, 15]. There are many processes that contribute to CM, but the most notable is impact ionization, which has been studied in great detail over the last two decades [14, 16–22].

The building blocks of this work are novel methods in describing, explicitly, carrier multiplication beyond the non-interacting electron and hole, while also including competition with phonon-mediated decay processes. This process was previously described in ref [23] and further improved in ref [24]. In development of this method, it has been applied to only a small amount of nanoscopic systems to investigate charge-transfer mechanisms and quantum efficiency. Here we employ the method, with some improvements, to a wider range of geometries to investigate its robustness and transferability to varied electronic structures and symmetries (i.e., localized and delocalized).

Our goal in this work was to perform a survey-type analysis of various CNTs with and without SP^3-hybridization surface defects to calculate quantum efficiency (QE) in all cases. We chose an array of CNTs that allow for comparison of diameter and chiral angle effects. In addition, we explore two binding configurations for the pair of covalent attachments that comprise a defect that show localization in one case and pristine-like delocalization in the other. With this sampling of systems, we hope to show the promise of SP^3-hybridized defects in applications to light-harvesting solar cells by decreasing previously high-threshold QE in pristine CNTs to low-threshold QE in defected CNTs; thereby, dramatically increasing their use as light harvesters [23, 24].

1.2. Model and Methods

The pristine CNTs were constructed using the Visual Molecular Dynamics (VMD) package [25]. Table 1.1 lists the details of the geometries used for the pristine tubes prior to optimization with DFT. Four additional geometries were also optimized: O+ and P+ defect configurations using Cl/Cl on pristine (6,2) and (10,5). See Fig. A.1 for a visual description of the defect orientation in O+ and P+ configurations. In addition, refer to ref. [26] for a more complete description of single-defect geometries and theoretical/experimental results.

Table 1.1. Geometry details of initial pristine systems used as input to geometry optimization.

Chirality	# Unit Cells	# Atoms	Length (nm)	Diameter (nm)	Chiral Angle (Deg.)
(10,5)	3	420	3.36	1.036	19.1
(11,0)	6	660	2.56	0.861	0
(6,5)	1	364	4.07	0.747	27
(9,1)	1	364	4.07	0.747	5.2
(6,2)	3	312	4.59	0.565	13.9

DFT was used to obtain the optimized ground state geometry and was carried out by the Vienna *ab initio* Simulation Package (VASP) using the Perdue-Burke-Ernzerhof (PBE) generalized gradient functional with the core electrons modeled using projector-augmented wave (PAW) pseudopotentials [27–35]. The simulation cell was subjected to periodic boundary conditions in all directions, and only the Γ-point was calculated. At least 8 Å was used to separate periodic images in the x- and y-directions to avoid strong cell-image interactions not along the tube axis in the z-direction.

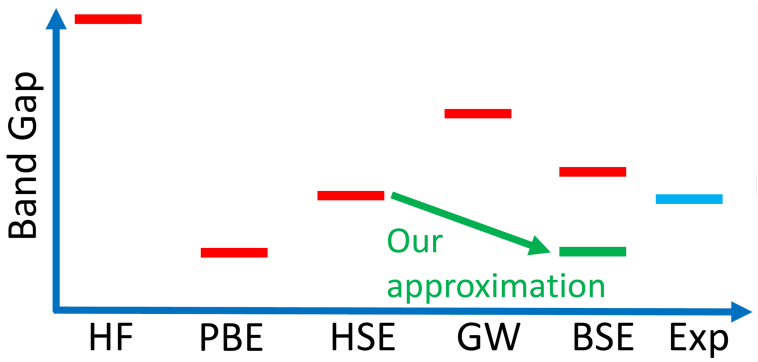

Figure 1.1. In our approximation, we take the HSE06 functional to give semi-accurate single-particle orbitals as a substitution for a full GW quasi-particle calculation. In turn, this redshifts our single-particle energies in comparison and is the main drawback of our methods. However, this redshift is shown later to be systematic and gives high precision energies for all systems (i.e., the standard deviation is small when comparing the redshift across all systems).

Once the geometry was optimized, a single-point calculation was performed using the HSE06 range-corrected functional [36–38]. This was done to obtain a more accurate electronic structure for input into the many-body formalism. This functional is to provide a better approximation to GW-level of theory and, as a result, opens the HOMO-LUMO gap compared to the PBE functional [39]. For visual aid to this approximation, see Fig. 1.1.

Using the output from the sinlge-point HSE06 calculation, we compute excitonic wavefunctions Ψ^{α}_{eh} via the Bethe-Salpeter Equation (BSE) in the Tamm-Dancoff approximation and then use those wavefunctions as input into the Boltzmann Transport Equation (BE) to obtain quantum efficiency (QE) [40, 41]. We will outline the general steps here, but for a more detailed explanation of procedure and approximations, see refs [23, 24, 42, 43].

$$(E^{\alpha} - |\epsilon_e - \epsilon_j|)\Psi^{\alpha}_{eh} = \frac{4\pi e^2}{V}\sum_{e'h'}(2K_{Exch} - K_{Dir})\Psi^{\alpha}_{eh} \tag{1.1}$$

where K_{Exch} and K_{Dir} are the direct and exchange operators represented in the Kohn-Sham basis [43].

$$K_{Exch}(e,h;e'h') = \sum_{\mathbf{q}\neq 0}\frac{\rho_{eh}\rho^{*}_{e'h'}}{|\mathbf{q}|^2} \tag{1.2}$$

$$K_{Dir}(e,h;e'h') = \sum_{\mathbf{k},\mathbf{p}\neq 0} \rho_{ee'}(\mathbf{k})\big[|\mathbf{q}|^2 - \Pi(0,\mathbf{k},\mathbf{q})\big]^{-1}\rho^*_{hh'}(\mathbf{q}) \tag{1.3}$$

$$\rho_{ji}(\mathbf{q}) = \sum_{\mathbf{k}} \phi^*_{\mathbf{j}}(\mathbf{k}-\mathbf{q})\phi_{\mathbf{i}}(\mathbf{k}) \tag{1.4}$$

where $\phi_i(\mathbf{k})$ is the i^{th} single-particle Kohn-Sham eigenfunction evaluated at the $\mathbf{k^{th}}$ reciprocal lattice vector.

$$\begin{aligned} \phi_i(\mathbf{k}) &= \frac{1}{\sqrt{V}}\int_V d\mathbf{x}\ \phi_i(\mathbf{x})e^{-i\mathbf{k}\cdot\mathbf{x}} \\ \phi_i(\mathbf{x}) &= \frac{1}{\sqrt{V}}\sum_{\mathbf{k}} \phi_i(\mathbf{k})e^{i\mathbf{k}\cdot\mathbf{x}} \\ \mathbf{k} = 2\pi\big(\frac{n_x}{L_x},\frac{n_y}{L_y},\frac{n_z}{L_z}\big),\ n_x,n_y,n_x &= 0,\pm1,\pm2,... \end{aligned} \tag{1.5}$$

$|\mathbf{q}|^2 - \Pi(0,\mathbf{k},\mathbf{q})$ is part of the screened Coulomb potential in the random phase approximation (RPA), and $\Pi(0,\mathbf{k},\mathbf{q})$ is the polarization evaluated at zero frequency (i.e., the static limit). The general form of the RPA polarization $\Pi(\omega,\mathbf{k},\mathbf{q})$ can be written as

$$\Pi(\omega,\mathbf{k},\mathbf{q}) = \frac{8\pi e^2}{V\hbar}\sum_{ij}\rho_{ij}(\mathbf{k})\rho_{ji}(\mathbf{p})\left(\frac{\theta_{-j}\theta_i}{\omega-\omega_{ij}+i\gamma} - \frac{\theta_j\theta_{-i}}{\omega-\omega_{ij}-i\gamma}\right) \tag{1.6}$$

$$\sum_i \theta_i = \sum_{i>HOMO},\quad \sum_i \theta_{-i} = \sum_{i\leq HOMO} \tag{1.7}$$

where the θ terms denote summing convention in this work.

Once excitonic wavefunctions Ψ^{α}_{eh} are acquired, and *en route* to MEG, we compute exciton-to-biexciton rates

$$R^{\gamma}_{\alpha\beta} = (R^p + R^h + R^p_{sh} + R^h_{sh})\delta(\omega_\gamma - \omega_\alpha - \omega_\beta) \tag{1.8}$$

$$R^p = \frac{4\pi}{\hbar^2}\left|\sum_{ijkln}\theta_{-l}\theta_n\theta_{-i}\theta_j\theta_k\ \ W^{\omega_\alpha}_{jlnk}(\Psi^{\beta}_{ln})^*\Psi^{\gamma}_{ij}(\Psi^{\alpha}_{ik})^*\right|^2 \tag{1.9}$$

$$R^h = \frac{4\pi}{\hbar^2}\left| \sum_{ijkln} \theta_l\theta_{-n}\theta_i\theta_{-j}\theta_{-k} \;\; W^{\omega_\alpha}_{jlnk}\Psi^\beta_{nl}(\Psi^\gamma_{ji})^*\Psi^\alpha_{ki} \right|^2 \tag{1.10}$$

$$R^p_{sh} = \frac{2\pi}{\hbar^2}\left| \sum_{ijkln} \theta_{-l}\theta_n\theta_{-i}\theta_j\theta_k \;\; W^{\omega_\gamma-\omega_{ni}}_{jlkn}(\Psi^\beta_{ln})^*\Psi^\gamma_{ij}(\Psi^\alpha_{ik})^* \right|^2 \tag{1.11}$$

$$R^h_{sh} = \frac{2\pi}{\hbar^2}\left| \sum_{ijkln} \theta_l\theta_{-n}\theta_i\theta_{-j}\theta_{-k} \;\; W^{\omega_\gamma-\omega_{in}}_{jlkn}\Psi^\beta_{nl}(\Psi^\gamma_{ji})^*\Psi^\alpha_{ki} \right|^2 \tag{1.12}$$

$$W^\omega_{jlnk} = \sum_{\mathbf{q}\neq 0} \frac{4\pi e^2}{V}\frac{\rho^*_{kj}(\mathbf{q})\rho_{ln}(\mathbf{q})}{q^2 - \Pi(\omega, -\mathbf{q}, \mathbf{q})} \tag{1.13}$$

where we now take the dynamic polarization to the screening of the Coulomb interaction, but we take only the diagonal components for computational ease. Note the θ sign convention for summing over Kohn-Sham indices and that $\omega_{ij} = |\epsilon_i - \epsilon_j|$, which is the non-interacting eh transition energy.

Using the same notation above for exciton state labels, we can write down the form of the Boltzmann Transport Equation (BE) in terms of exciton state occupations, including MEG, phonon-dissipation, and exciton transfer terms:

$$\dot{n}_\gamma = C_{phonon}[n] + \sum_{\alpha,\beta} C_{MEG}[n] \tag{1.14}$$

$$n_\alpha \frac{dn_\beta}{dt} + n_\beta \frac{dn_\alpha}{dt} = -\sum_\gamma C_{MEG} \tag{1.15}$$

$$C_{MEG} = R^\gamma_{\alpha\beta}\big(n_\alpha n_\beta - n_\gamma(n_\alpha + n_\beta + 1)\big) \tag{1.16}$$

In this work, we choose not to explicitly write the C_{Phonon} terms, as they are cumbersome and may detract further from the main purpose of this work. They can be found explicitly in ref [24]. The main methodological difference between this work and previous is that the full, static polarization is used here instead of the diagonal approximation (i.e., $\Pi(0, \mathbf{k}, \mathbf{p})$), which is expected to improve the accuracy of the exciton states, which we hypothesize will have a large impact on

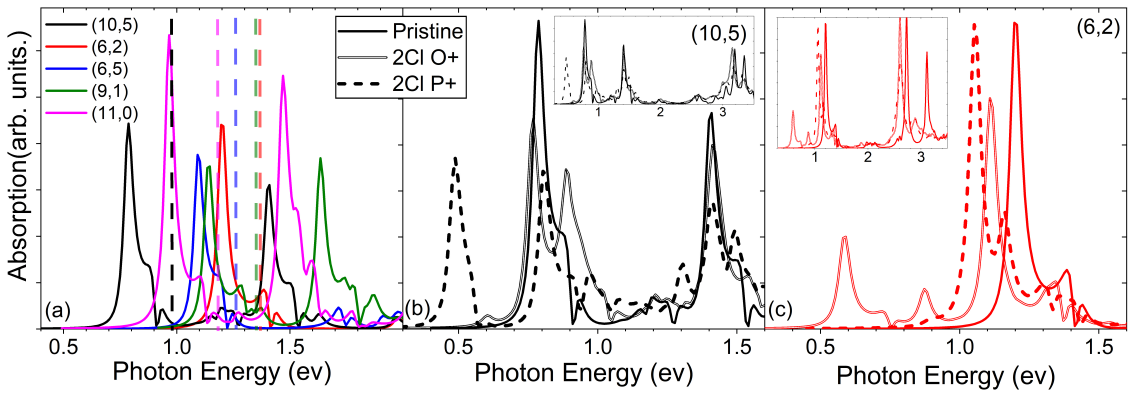

Figure 1.2. Absorption rates for various pristine (a) and functionalized (b,c) CNTs. Vertical dashed lines correspond to experimental results for low-energy absorption at the E_{11} band. Note redshift dependence is dictated by both chirality and configuration of defects, therefore, all excited state properties will be governed by these same parameters.

MEG, even if those subsequent steps only include the diagonal approximation to the dynamic polarization.

We then solve the Boltzmann Transport Equation (BE) for the time-dependent exciton and biexciton occupations. We then compute quantum efficiency (QE) at the steady-state limit.

$$QE = \sum_i n_i(t) + 2\sum_{ij} u_{ij}(t), \quad t \to \infty \tag{1.17}$$

where $u_{ij}(t)$ is the biexciton state comprised of two, non-interacting exciton states as $u_{ij}(t) = n_i(t)n_j(t)$.

1.3. Results and Discussion

In this work, we aim to explore excited state properties and processes in an array of pristine and functionalized CNTs. Methods have been developed that rely on ground state density functional theory (DFT) as input to form a basis for higher-order calculations. We perform a quantitative analysis of the accuracy of this many-body method as applied to CNTs of varying diameter and chiral angle, as well as CNTs that have been functionalized with SP^3-hybridization defects. The obvious first observable to examine is the absorption spectra of each geometry, which can be obtained immediately after solving the BSE and obtaining the exciton wavefunctions Ψ^{α}_{eh}.

Fig. 1.2 shows computed absorption spectra for all CNT geometries studied. In addition, we compare to experimental (given by ref [44]) values for the E_{11} energies, which provide a benchmark

for error in the methodology. We only include spectra up to 2.0 eV for two reasons: (I) the single-particle energy window included in the basis is around 3.5 eV and so the excitonic wavefunctions and energies may be not trustworthy above ∼2.5-3.0 eV and (II) for applications of CNTs to multiple exciton generation (MEG) requires examination of the lowest-energy states, well within the characteristic CNT $E_{11/22}$ absorption bands. The inset in Fig. 1.2(b,c) show the absorption rates up to 3.5 eV for reference. We see there to be a large region (∼1-1.5 eV) of dark states. This further allows us to concentrate our attention to the sub-2-eV region for most future discussion.

The ordering of the redshift in defected CNTs is known to be related to the MOD(n-m,3) value for each chirality [13]. Therefore, it is expected that (10,5) with a defect in the P+ defection will be more redshifted in comparison to its pristine than the O+ configuration. In addition, the (6,2) should produce the opposite trend, as the MOD value is 1 instead of 2. This is evident from the absorption plots shown in Fig. 1.2(b,c).

Table 1.2. E_{HL} and E_{11} values for all pristine CNTs compared to experimental data. All values are in eV.

System	E_{HL}^{HSE06}	E_{Gap}^{BSE}	E_{11}^{BSE}	E_{11}^{WB}	ΔE_{11}	E_{22}^{BSE}	E_{22}^{WB}	ΔE_{22}
(10,5)	0.91	0.78	0.80	0.993	0.193	1.41	1.574	0.164
(11,0)	1.13	0.96	0.97	1.196	0.226	1.48	1.665	0.185
(6,5)	1.22	1.09	1.11	1.270	0.160	2.10	2.190	0.09
(9,1)	1.31	1.13	1.15	1.359	0.209	1.62	1.794	0.174
(6,2)	1.31	1.03	1.21	1.387	0.177	2.72	2.963	0.243

In Table 1.2, we tabulate the ground state HOMO-LUMO gap energies for HSE06 for pristine CNTs as well as the excitonic gap produced by the BSE. The values reported for the excitonic gap E_{Gap}^{BSE} are all redshifted shifted from the ground state gap E_{HL}^{HSE} by 150 meV on average, excluding (6,2), which is shifted by 280 meV. In addition, we of course recover the "particle in a box" trend of increasing gap (and E_{11}, E_{22}) energy with decreasing diameter (top to bottom in Table 1.2). The methods used in this work to compute the excitonic wavefunctions and energies is known to overbind the eh pair and redshift the energetic properties. This is seen by a systematic redshift in the E_{11} energies in comparison to the experimental data. The average redshift in energy from experiment for the first absorption peak ΔE_{11} is 193 ± 23 meV, where the standard deviation of the redshifts are of the order of thermal energy at room temperature. For the second absorption

band ΔE_{22}, the mean redshift is 171.2 ± 49 meV. These metrics imply that the precision of this method is relatively high and trustworthy, at least for CNT or CNT-like systems. The accuracy is also reasonable, as there is simply a 0.2 eV redshift from the experimental value, and there are known approximations that contribute to this systematic error in addition to solvent effects in experimental values. The most important approximation is the use of HSE06 as a substitute for a full GW calculation, which will further blueshift the single-particle states in comparison to HSE06 (see Fig. 1.1). Another important approximation is the truncation of the plane-wave basis to $\sim 5\text{E}^5$ (down from 1-4E^6) in order to efficiently invert the polarization matrix within the direct matrix $K_{Dir}(e,h;e',h')$. This is a trade-off in comparison to the diagonal approximation used in previous works, where all plane-waves can be kept. It is not yet known which procedure is more accurate; however, we expect that the full polarization, even though truncated, provides more useful information about the anisotropy of the quasi-one-dimensional system, as long as the real-space resolution captures the smallest bond length.

Table 1.3. Various energy values for defects CNTs, where $\Delta\text{E}_{11} = \text{E}_{11}^{Pristine} - E_{11}^{*}$. All data is given in eV.

System	E_{HL}^{HSE06}	E_{Gap}^{BSE}	$\text{E}_{11}^{*,BSE}$	ΔE_{11}^{*}
(10,5) 2Cl O+	0.70	0.60	0.70	0.10
(10,5) 2Cl P+	0.56	0.48	0.48	0.32
(6,2) 2Cl O+	0.75	0.57	0.57	0.64
(6,2) 2Cl P+	1.18	0.88	1.08	0.13

For functionalized (6,2) and (10,5) CNTs, we tabulate E_{HL}^{HSE}, E_{Gap}^{BSE}, and E_{11}^{BSE} for each geometry in Table 1.3. However, we do not compare to experimental data, as the chemical species used to functionalize the CNTs are not widely found in experiment and were used to reduce the computational cost of these calculations, which scales poorly with computational cell volume as well as the number of additional electrons. However, we know from previous reports that the defect species modifies the redshift not by more than 300 meV from another species. The chlorine attachments we have chosen here represent some of the most redshifting species, which is related to chlorine's electronegativity. In addition, we do not expect these systems to be any more sensitive to the methodological redshift than the pristine systems. However, this is not fully known. Comparing the defect-associated lowest-energy transitions to those of the pristine ΔE_{11} suggest similar degrees

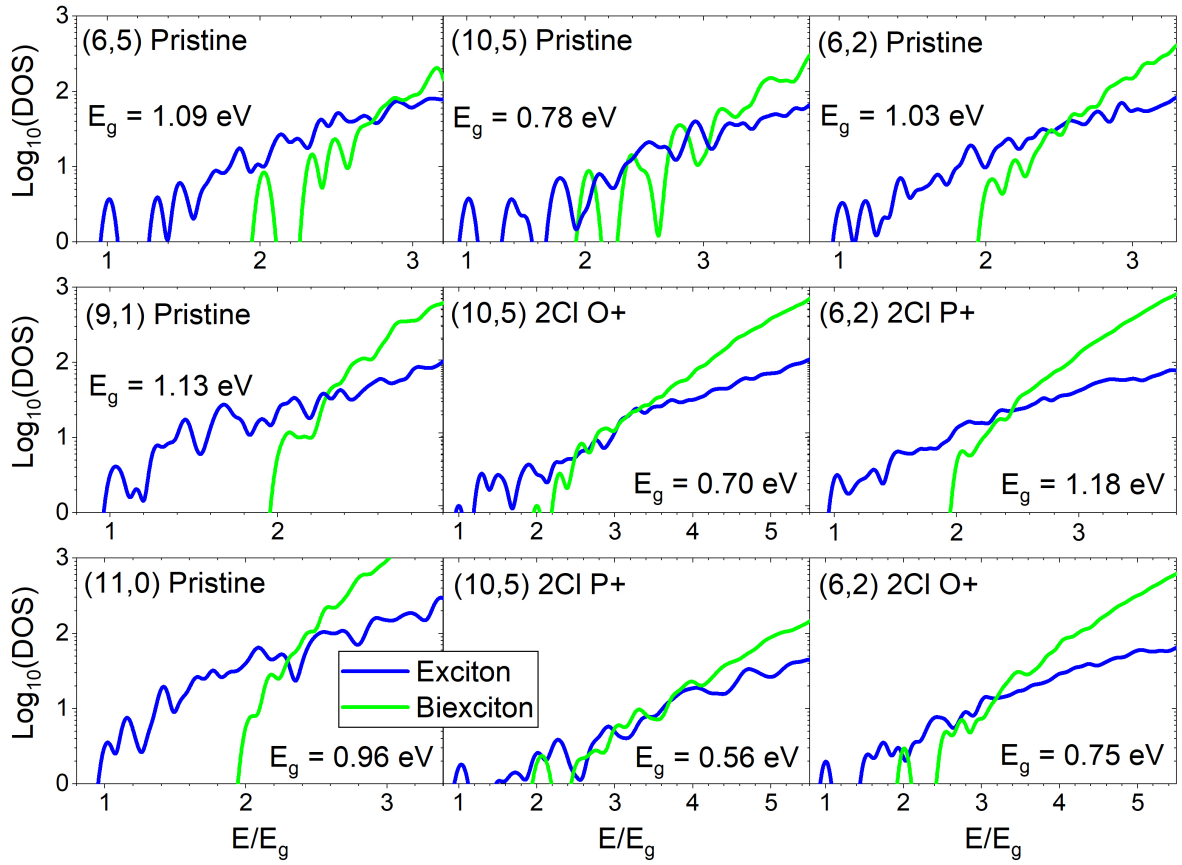

Figure 1.3. Exciton (blue) and biexciton (green) DOS for various pristine and functionalized CNTs. The functionalized geometries are arranged such that the middle row produces less redshift than the bottom row. At $2E_g$, the biexciton DOS of the most redshifted defect configurations is equal to or higher than exciton DOS, indicating optimal conditions for minimum-threshold QE. Note the units of DOS are inverse energy and that thermally broadened δ-functions (Gaussian width = 25 meV) were used.

of redshift as expected. In particular, the (6,2) CNT is much more narrow than (10,5) and so upon functionalizing in the most redshifted configuration, the energy shift is much larger. However, functionalizing in the least redshifting configuration produces similar redhisfts between CNTs.

We now show in Fig. 1.3 the exciton and biexciton density of states (DOS) for each geometry. Thinking ahead to calculating the exciton-to-biexciton decay rates, the amount of biexciton states that are available to be occupied within some small energy interval should increase the chance of biexciton formation within that energy interval that decayed from a higher-energy exciton state. Therefore, the complex interplay between the exciton DOS and the biexciton DOS will partially dictate the the MEG threshold (i.e., the lowest-energy, non-negligible exciton-to-biexciton rate),

which has a theoretical minimum at $2E_g$. We see in pristine (6,5) that the biexciton DOS is nearly as high as the exciton DOS at the threshold, which is favorable for low-energy biexciton formation. Similarly, looking at the pristine (10,5) panel, we notice that the biexciton DOS is actually larger than the exciton DOS, which should indicate that there will be non-negligible rates at the threshold. However, this is not what we see in computation of the rates shown in Fig. 1.4(a). In fact, for all pristine CNTs, except for (6,5) where we see rates at $2E_g$, we see negligible rates until $\sim$2.4 E_g. The reason for this is currently unknown.

In examination of the defected CNTs in Fig. 1.3, we see that the most redshifted geometries produce appreciable biexciton DOS (in comparison to the exciton DOS at the same energy) near the threshold. These DOS looks vastly different from those of pristine and of the less redshifted functionalized geometries. Looking to the analogous curves of Fig. 1.4(b,c), we see that the defected CNTs clearly have non-zero rate of formation at the threshold. For (10,5) 2Cl P+ (Black,dashed), we see a very large rate compared to (10,5) 2Cl O+, for which there is almost none until 2.3 E_g. The reason for this is also unknown. In the geometries of (6,2) with defects, we see negligible differences between O+ and P+ configurations. Although, overall, the P+ geometry has larger rates. At this time, we have no explanation for this.

There may be concern over the non-zero rates under the $2E_g$ threshold; however, this is due to the finite-width effects of the rates calculations as well as the interpolation function used to smooth the data. These rates can be ignored and can be shown to be zero without the finite width and interpolation effects.

In order to allow for competition between biexciton formation and phonon absorption processes in the BE, we computed the phonon absorption and emission rates in the harmonic approximation, including two-phonon couplings, which are needed to overcome the electronic sub-gaps seen in these systems. See Fig. A.2 for phonon density of states (DOS) for all pristine CNTs (a) and the two (10,5) functionalized CNTs.

Once solving the BE for each exciton state, we smooth the data by averaging within a thermal-energy-sized (i.e., $k_BT \sim 25meV$) bin and interpolate between bins. Fig. 1.5 shows QE for three systems: Pristine (10,5) and (6,5) and functionalized (10,5) with 2Cl in the P+ configuration. Here we compute the internal quantum efficiency (IQE) of the system, where we assume that one photon produces an exciton and subsequently decays in energy through MEG or vibronic processes.

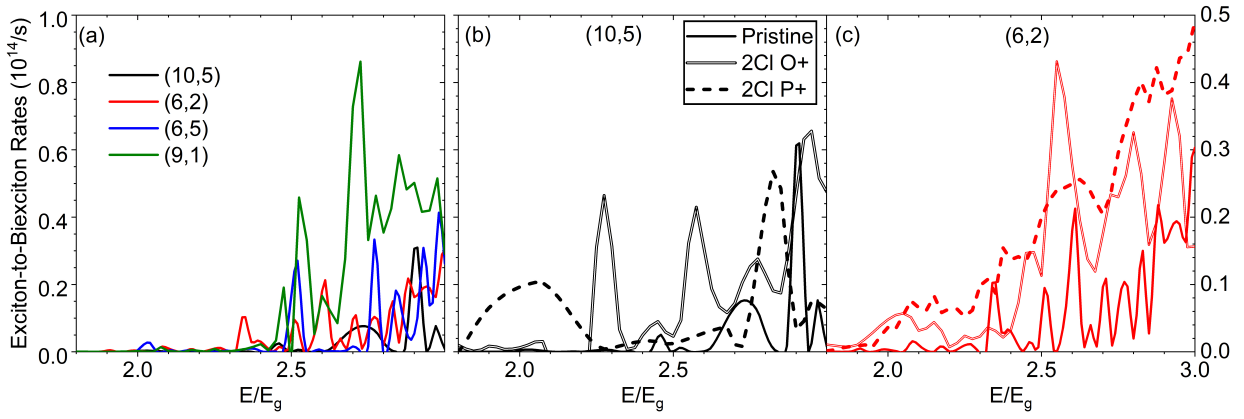

Figure 1.4. Exciton-to-biexciton rates for various pristine (a) and functionalized (b,c) CNTs. Keeping in mind, these rates are only part of the picture without considering competition with phonons, all pristine CNTs except (6,5) have negligible biexciton formation rates until about 2.4 E_g. Upon functionalization, in three of the four cases, the biexciton formation threshold is lowered to its minimum of $2E_g$. In all cases, the overall rates are increased upon functionalization due to the increased DOS. (10,5) 2Cl O+ produced a reduction but only from 2.5 E_g to 2.3 E_g. This may be a consequence of both diameter and configuration, as the O+ in (10,5) produces minimal redshift from the already low-energy pristine exciton. It is hypothesized that the least redshifted configuration is the least effective configuration to reduce the MEG threshold from pristine.

We note that external quantum efficiency (EQE) is sometimes reported in experiment, where this QE is less than or equal to IQE at some given energy and is considering the possibility of non-absorbed photons incident on the system. In our numerical experiments, we assume that the incident photon has a probability of 1 to be absorbed by the system.

$$EQE = \frac{Excitons\ Produced}{Incident\ Photon} \tag{1.18}$$

$$IQE = \frac{Excitons\ Produced}{Absorbed\ Photon} \tag{1.19}$$

Similarly to the biexciton formation rates shown in Fig. 1.4, we see that (6,5) produces non-zero carrier multiplication very near to the threshold of $2E_g$; whereas, say, (10,5) is negligible until around 2.4 E_g. However, as expected, upon functionalization of the (10,5) CNT, we see that there is non-negligible carrier multiplication at the threshold. However, we note that it is somewhat low, but even low QE can lead to large gain in overall efficiency, and we expect that increasing the density of defects would lead to further increase in QE. Recall that pristine (6,5) and (9,1) share

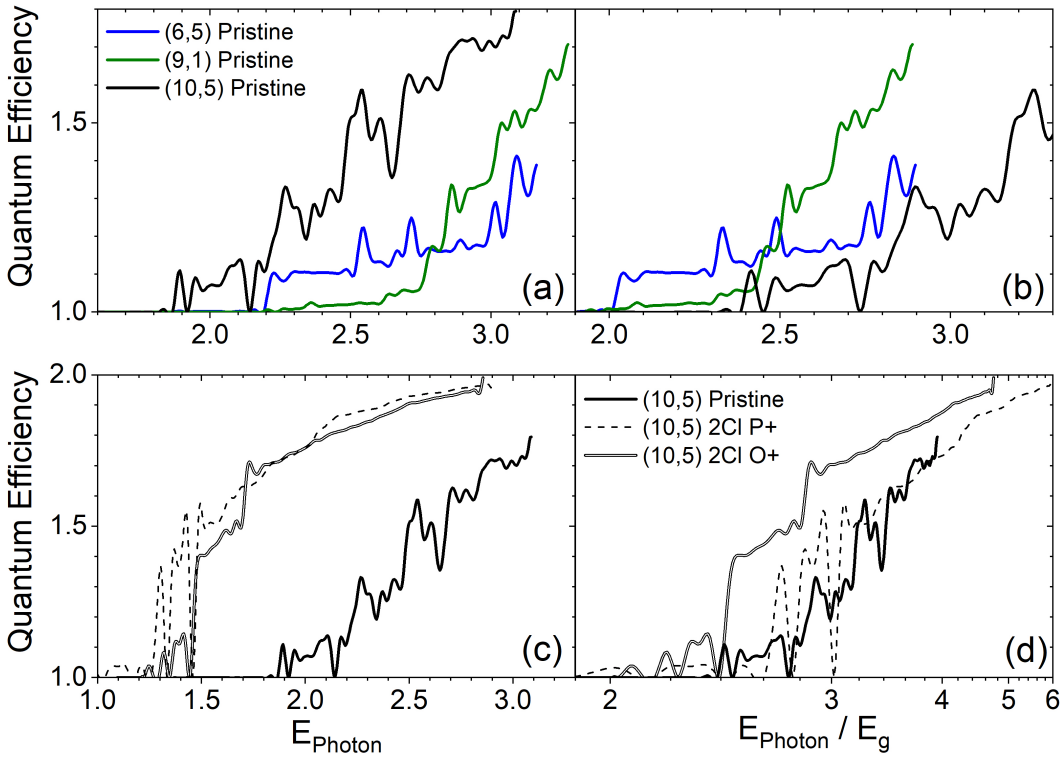

Figure 1.5. Internal quantum efficiency for a subset of systems studied in this work: Pristine (10,5), (6,5), and (9,1) as well as Cl/Cl functionalized (10,5) in O+ and P+ configurations. Panels (a,c) are shown as a function of photon energy. Panels (b,d) show the same information but in energy normalized by the optical gap E_g.

equivalent diameter but have contrasting chiral angles of roughly 27 and 5°, respectively. Our results show that both CNTs have some QE at the threshold, but (6,5) dominates. This suggests a chiral angle dependence on the QE, but our limited data does not allow to make any deeper conclusions.

Although there are no direct experimental comparisons for the numerical data produced here, we can (very loosely) compare to the work of Wang and coworkers, where they show excitonic populations at a limited number of excitation energies. This data, however sparse, aligns well with our results for the (6,5) CNT, where they claim two QE points at 2.5 E_g and 3E_g to be 1.1 and 1.3, respectively. Our results seem to be in agreement at 1.15 and 1.35 (at 2.8 E_g), respectively.

1.4. Conclusion

In conclusion of this chapter, we reiterate the achieved and soon-to-be achieved goals of this work as well as suggested further work needed to flesh out open questions that cannot be answered

with our results. We have successfully investigated an array of CNT systems, both pristine and with SP^3-hybridized defects for their properties relating to carrier multiplication for use in solar cells. We have done this by using DFT-based MBPT methods including excitonic effects and phonon-mediated dissipation processes to calculate QE for each system. We note that most pristine CNTs do not show large QE until $2.4E_g$, which is unfavorable for application. (6,5) is excluded from this trend, as it shows appreciable QE at the threshold of $2E_g$. Upon functionalization, we see the QE threshold decrease from 2.4 to 2.0 E_g and expect similar trends for all CNTs. We yet do not know the extent to which the configuration effects the QE, nor do we understand fully the effects of chirality and diameter. Further insight is needed, which includes producing QE for the larger array of CNTs. Moreover, functionalization in all six configurations of each CNT is needed for the most thorough and deep investigation of carrier multiplication processes within these systems.

2. INTERACTING PAIRS OF SURFACE DEFECTS ON CARBON NANOTUBES

2.1. Introduction

Single-walled carbon nanotubes (CNTs) have unique photoemission properties after covalent functionalization for applications to highly-tunable single-photon emitters in telecommunications wavelengths [4, 45–47]. Pristine CNTs do not achieve appreciable photoemission due to dark, low-energy excited states, and the optical gaps for most CNTs are not yield emission in these low-energy [48, 49]. However, post-functionalization via an SP^3-hybridization defect (comprised of a pair of functional groups attached to a single carbon ring), the lowest-energy state becomes bright, dramatically increasing photoluminescence (PL) efficiency [4–6, 11, 26, 49–52]. Furthermore, the electronic and geometric properties of the functional groups, i.e., orientation about the CNT axis and electronegativity, govern the tunability of the redshifted energy state for a given chirality [4,11,26,51]. Kwon and coworkers experimentally established that the redshift in energy of the new, emissive states correlates linearly with the effective inductance parameter, which varies depending on the electronegativity of the chemical groups [11]. This relationship was recently reinforced by computational results which show the redshifitng effects of varying chemical groups and relating this redshift directly to the local charge on the CNT surface atom [51]. Additionally, computational reports have repeatedly shown that the configuration of the defects with respect to the CNT axis plays the largest role in redshifting of the emissive defect state [13, 26, 51].

While these defects give a wide range of tunability in emission energies, only select computational configurations have been mapped to experimental samples, with the others lost within the characteristic E_{11} excitonic absorption band, the first van Hove singularity in these quasi-one-dimensional carbon structures that corresponds to the lowest-energy pristine emission dictated solely by the environment and diameter of the CNT [49, 50, 53, 54]. In experimental spectra, there are two defect-associated emission bands, labeled as E_{11}^* and $E11^{*-}$ in recent literature, where each are redshifted from the E_{11} band, with E_{11}^* defined to be more redshifted than E_{11}^* [4,5,13,26,51,55]. These two bands presumably correspond to varied binding configurations [4, 51, 55] At low temper-

atures, these defect-associated peaks in single-tube spectra become vary scattered in energy and shape, which may give insight into multiple contributing defect configurations present at varying probabilities and may be averaged out in room temperature solution spectra [55].

Novel recent literature has been experimentally targeting methods to control the locations and examine the effects of spatially localized defects [9,56]. Zheng and coworkers have used ss-DNA with varying amounts of guanine content to control the patterning, and therefore the concentration, of defects [56]. and coworkers have recently attempted to show the interaction between nearby defects using high-resolution spectroscopy [9]. These pioneering works still leave many open questions about how nearby defects may interact and on what length scales these interactions play a role in exciton formation and photoemission. In the latter work, the inter-defect spacing is reported on the order of 0.1 microns, which is much larger than the known defect-localized exciton size of roughly 2 nm as well as the mean exciton diffusion length of roughly 10 nm [9, 57]. The high-resolution spectra produced by the supposed interaction between these defects shows emission energy shifts of up to 20 meV, which may arise from the varied environments of the defects and not their direct interaction.

From both a theoretical and experimental standpoint, the concept of interacting defects on CNTs, their resulting exciton formation, interaction length scales, and subsequent photoemission properties remain rather unexplored. For pristine CNTs, the concept of exciton size has been thoroughly studied and was easily extended for single defects [53, 54, 57–65]. In this case, studies have shown that redshifted excited states correlate to the reduced size (localization) of the exciton due to an effective one-dimensional potential well produced by the defect [13,51,52,55]. In the case of two defects, the exciton may be shared, effectively becoming more delocalized over the length of the tube, or it may be drawn toward one defect, exhibiting similar localization as the single-defect system. In either case, excitonic properties will depend on the defect-defect coupling, presumably varying with defect configuration, composition, and defect-defect separation distance.

In a first approximation, a simple approach to modeling interacting systems called molecular exciton theory (also referred to as Kasha's exciton model) can be employed [66–68]. This effective Hamiltonian method couples two or more independent systems by some perturbative interaction Hamiltonian, often of purely Coulomb type, with applications to molecular spectroscopy

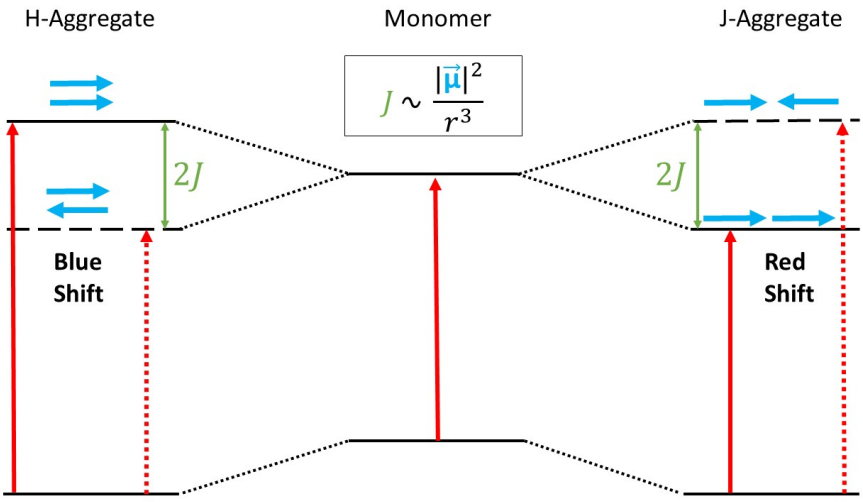

Figure 2.1. Transition state diagram according to general Kasha theory on HJ aggregates. H-aggregates are formed by stacking two "monomers", producing blue shifted transition energies in comparison to the single aggregate, stemming from the fact that parallel transition dipole moments are stacked. J-aggregates are formed similarly by "head-to-tail" orientation instead of stacked, which switches the bright and dark states, producing a red shifted transition, respectively.

and absorption band splitting based on geometry [69–71]. This method is frequently employed to describe interacting chromophores and highly-conjugated molecules [69–75].

Kasha's seminal work illustrates how the orientation of two interacting molecular aggregates causes exciton splitting. The original theory describes two classes of aggregates known as H- and J-type aggregates, where H-type is a "stacked" configuration of the transition dipoles and J-type is "head-to-tail" [66, 67, 69, 70]. Fig. 2.1 shows a cartoon schematic of HJ aggregates and respective shifts in transition energies relative to that of the monomer. In the J-type geometry, and with respect to the monomer transition energy, the bright state is redshifted, and in the H-type geometry, the bright state is blueshifted.

Kasha's theory is derived within the point dipole approximation; thus, it is important to establish the theory's validity for a functionalized CNT. Previous reports have shown that pristine CNTs fail to be effectively modeled by the point dipole approximation due to their extremely delocalized electronic structure [58, 76]. However, as previously mentioned, CNTs with covalent defects undergo exciton localization to around 2 nm, rather than 10 nm. In addition, these previous works were analyzing interacting CNTs, and we would expect that interacting defects on the same

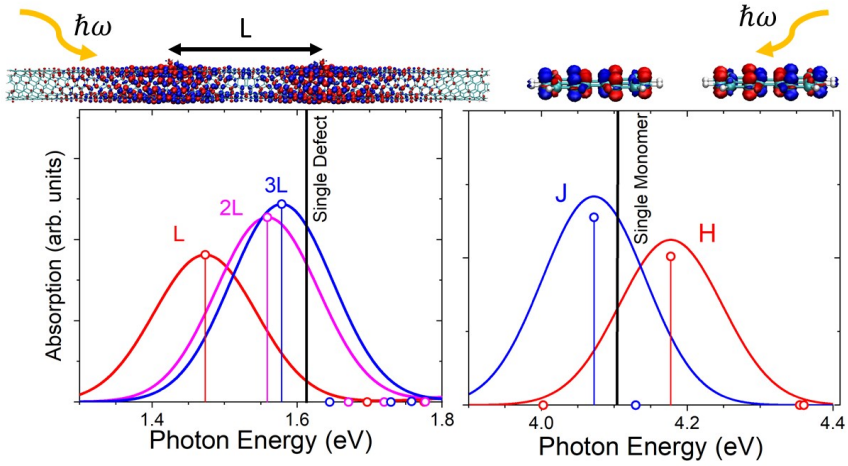

Figure 2.2. Carbon nanotubes (CNTs) carrying two or more covalent defects have strong similarities to interacting molecular aggregates that allow for splitting between excitonic states through dipolar interaction. We see increased tunability by modifying the separation distance between the defects, which allows for increased redshifting beyond the previous limit of diameter and configuration dependent thresholds.

CNT will be more weakly interacting than interacting CNTs due to the reduced dimensionality of the interaction, i.e, three-dimensional to quasi-one-dimensional.

In this chapter, we investigate interacting, localized excitonic states stemming from covalent SP3-hybridization defects on the surface of an experimentally relevant CNT with an effective Hamiltonian model in the point dipole approximation fit to time-dependent density functional theory (TD-DFT) data. We find that J-type defect-associated states are, in general, well-modeled by this approximation and show qualitative correspondence to a model system. However, H-type states are too well-coupled and would require additional interaction terms, such as Coulomb exchange and vibrational coupling, which has been formalized for other systems but not included in this work for brevity [69, 70]. See Fig. 2.2 for an example of CNTs as HJ aggregates alongside an ideal aggregate.

2.2. Methodology

Calculations were carried out on the (6,5) CNT, for its wide use in experiment, with three unit cells and a capping scheme that terminates with hydrogens in order to recover semi-infinite electronic structure [4,26,51,77]. We optimized the geometry with density functional theory (DFT) with the CAM-B3LYP/STO-3G functional. This level of theory has been shown to produce re-

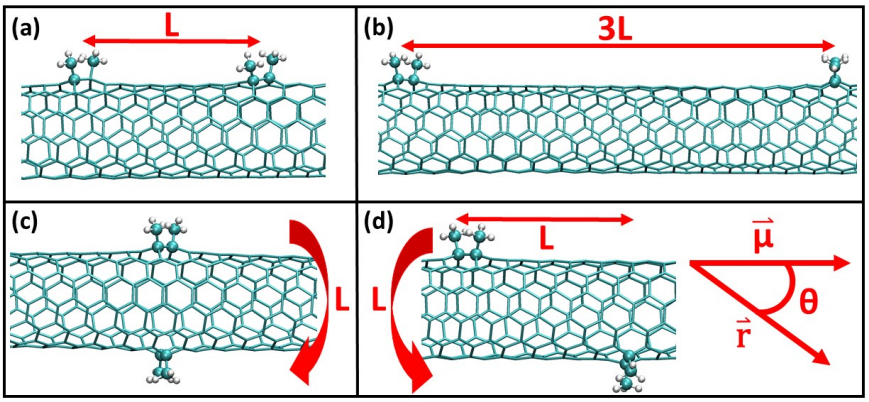

Figure 2.3. Four types of binding geometries for two pairs of defects, where L = 10 separating carbons. Binding geometries: (a) Axial L 11, (b) Axial 3L 31, (c) Circumferential L 12, and (d) Axial L Circumferential L 12.

sults in good agreement with experimental observations [26, 48, 77]. We then computed the singlet excitations using time-dependent DFT (TD-DFT). All calculations were performed using the Gaussian16 software [78]. Transition densities of the excited states were visualized using the Multiwfn package [79, 80].

We restrict this work to defects in ortho positions, as these are thought to be the most kinetically favorable structures; although, the analogous para configurations have not yet been fully ruled out as probable binding configurations and may require further study. As such, there are three possible binding configurations per defect, each labeled by its direction with respect to the tube axis. Following previous notation for the (6,5) CNT: L30 (Type 1) is along the chiral angle, L90 (Type 2) is nearly parallel with the tube circumference, and L-30 (Type 3) is -30 degrees off the tube axis [26]. For brevity, these three ortho positions will be denoted by 1, 2, and 3, respectively, which allows for a chirality-independent nomenclature. (Fig. A.3) shows a cartoon of all three configurations.

There are six independent ways to combine these three types of defects, as swapping their identities produces an equivalent system due to symmetry, i.e., ij = ji.

There are numerous ways to place (i.e., translate) a pair of defects on the surface of a CNT. Fig. 2.3 shows examples of four unique translations of two single-defect pairs studied in this work: Fig. 2.3(a) axial L, Fig. 2.3(b) axial 3L, Fig. 2.3(c) circumferential L, and Fig. 2.3(d) a combination

of axial and circumferential translations, where L is defined as half the CNT circumference (L = 10 Separating Carbons $\sim$ 1.3 nm). We chose to explore two types of directional translations: (I) axial, where the defects are translated on the same side of the CNT $\{\theta = 0°\}$ Fig. 2.3(d), and (II) circumferential, where the defects are translated on opposite sides of the CNT $\{\theta$: $(r_z \to \infty)$ $0 < \theta < 90$ $(r_z \to 0)\}$ Fig. 2.3(d) where r_z is simply the z-component of the defect-defect connecting vector. One can write down the effective exciton Hamiltonian coupling these two defect-associated excitonic states,

$$H = \begin{pmatrix} \omega_i & J_{ij} \\ J_{ij} & \omega_j \end{pmatrix}, \qquad \{i, j\} \in \{1, 2, 3\}, \tag{2.1}$$

where ω_i is the transition energy for a non-interacting defect of type i. In the most general case, where the defects are not chemically identical and produce spectrally dissimilar transition energies, J_ij is the coulomb coupling between the aggregates. The eigenvalues of this Hamiltonian are

$$E_{\pm} = \frac{\omega_i + \omega_j}{2} \pm \sqrt{\left(\frac{\omega_i - \omega_j}{2}\right)^2 + 4J_{ij}^2}, \tag{2.2}$$

which are interpreted as the expected transition energies of the coupled excitonic states given by the interaction Hamiltonian. So far, we have made no explicit assumption about the interaction between the states, only about how this interaction modulates the transition energies in a generic and simplified sense. In the first approximation to describe the coupling between uncoupled transition states, it is common employ a point dipole approximation such that

$$J_{ij} = \frac{1}{4\pi\varepsilon_o} \frac{(\vec{\mu_i} \cdot \hat{r})(\vec{\mu_j} \cdot \hat{r})}{r^3}, \tag{2.3}$$

where μ_i is the transition dipole moment of defect i and r is the dipole-dipole connecting vector, which is taken to be connecting the center of masses of each defect [66, 67, 69, 70]. This point dipole approximation is valid for dipoles that are small compared to the dipole-dipole separation distance. In applying this simple theory to defected CNTs, we may attempt to examine the, now non-degenerate, transition states appearing from the interaction Hamiltonian, where we may expect to see splitting on the order of J_{ij} between the two transition energies.

2.3. Results and Discussion

2.3.1. Ground State Properties

As a first look at understanding how defects interact with one another, an obvious first set of observables to examine are ground state energies, as they are readily available from DFT software and are encoded with many details of system. Fig. 2.4(a) depicts single-defect destabilization energies, where the total energy of the pristine system is subtracted from the total energy of the defected system. For each configuration, i.e., 1, 2, and 3, we label this arbitrary energy $\Delta 1$, $\Delta 2$, and $\Delta 3$, respectively. At infinite defect-defect separation, we expect uncoupled, non-interacting defects that act exactly like single defects. Fig. 2.4(b) shows destabilization energy for all combinations of two defects translated by axial L, 2L, and 3L as well as circumferential and both circumferential and axial. At the non-interacting limit, we expect that the destabilization energies of each defect will be additive. For example, the destabilization energy of a defect combination of type 31 could be well approximated by $\Delta 3 + \Delta 1$. The horizontal dashed line indicates this hypothesis for each combination of defect pairs. The first three columns of Fig. 2.4(b) show axial translation (i.e., $\theta \sim 0°$) at increasing distances of L, 2L, and 3L. One can see that the axial L translation does not closely follow this hypothesis, but the 2L and 3L translations become very close, indicating energetic decoupling. We can see that ground state energy decoupling occurs very quickly with increasing length and negligibly changes after 1.3 nm. In Fig. 2.4(c), the deviation from this hypothesis is shown by taking the difference between the destabilization energy of some combination in Fig. 2.4(b) and subtracting it from its hypothetical value (dashed line). With increasing separation, this value approaches zero for all combinations. Looking at the circumferential geometries (i.e., $\theta \sim 90°$), we see major deviation from this additive hypothesis, showing up to 0.26 eV in energy change through interaction between defects. This energy difference could be a result of both geometric and -orbital distortions as well as asymmetrical breaking of -orbital resonance around the tube. This wide range of energy separation may give rise to novel experimental techniques to attach defects in specific configurations for increased electronic structure tunability. The final unique translation of both axial L and circumferential L (i.e., $\theta \sim 45°$) seems to give results nearly opposite of the axial L geometries. This implies that axial separation is not the only parameter that governs these

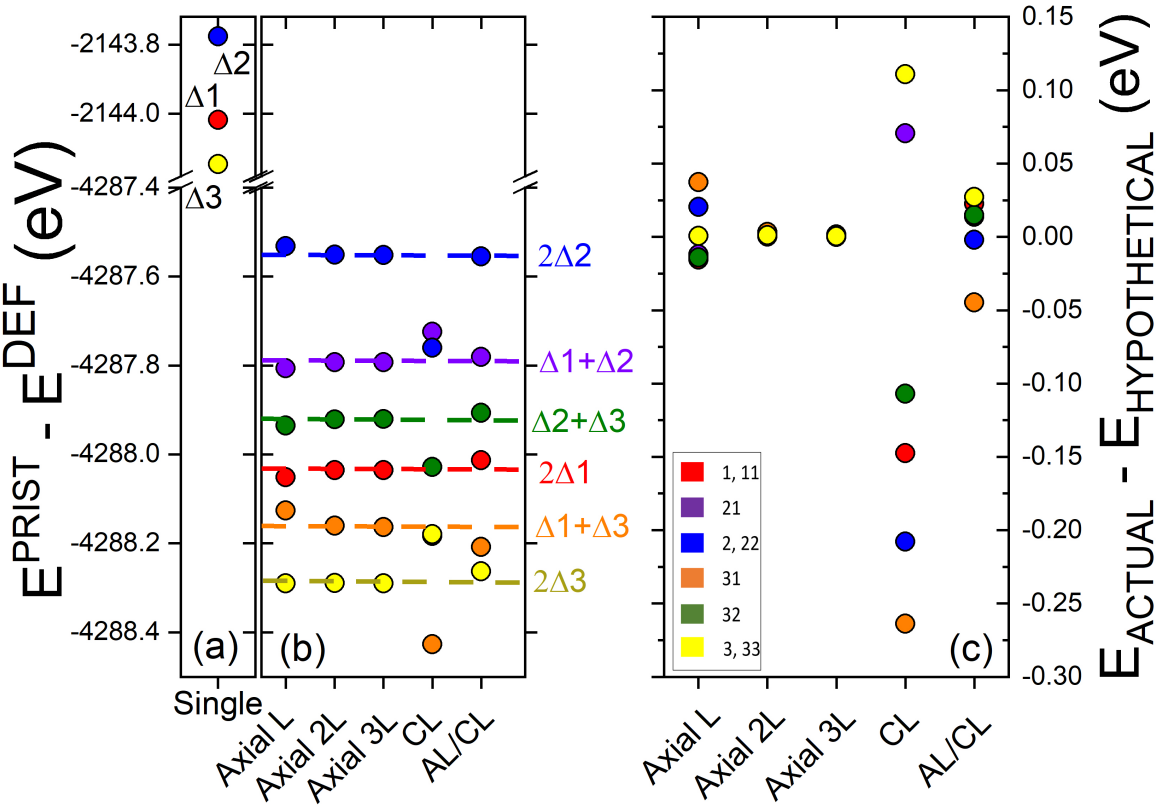

Figure 2.4. Thermodynamic stability of each geometry studied is shown here. (a) Single defect total energies are shown subtracted from the pristine total energy, which we label Δ1, Δ2, and Δ3, respectively. (b) All defect geometries calculated and their respective total energies, again subtracted from the pristine total energy. The dashed lines represent different additive combinations of Δ1, Δ2, and Δ3, which clearly show that the stability of defect pair combinations is simply the addition of the two defect pairs that comprise that combination. This becomes more and more accurate as the interaction (i.e. distance) between the defect pairs becomes weaker and weaker moving from Axial L to 3L. CL represent a circumferential translation of length L, and AL/CL represents an axial translation of length L followed by a circumferential translation of length L. (c) The deviation from this additive hypothesis is plotted. The circumferential configuration shows the most deviation from this trend, showing that some configurations are more stable than others.

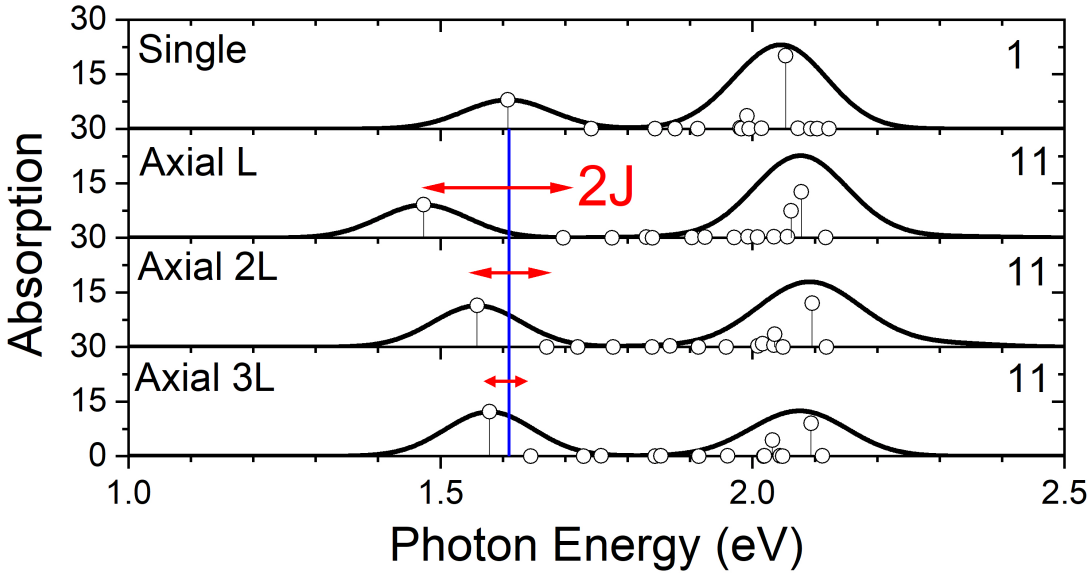

Figure 2.5. Absorption spectrum for four geometries, including both the bright pristine E_{11} transition (∼2.05 eV) and the bright (and dark) defect-associated transitions (∼1.4 – 1.7 eV). Single defect in the type-1 configuration as reference for the J coupling value. With increasing distance L, 2L, to 3L, we see an increase in J-splitting symmetry as well as a decrease in J-splitting magnitude. The splitting becomes more and more symmetric due to the increase in distance, which implies that the wavefunctions of each defect are becoming less overlapped and becoming more and more ideal to the simple Kasha model. In addition, since $J \sim 1/r^3$ in the point-dipole approximation, the magnitude of splitting decreases with increasing defect-defect distance r. Note that the vertical axis scale represents unitless oscillator strength and not absorption, which has arbitrary units.

systems. Most likely, the extended -conjugation will play a role and introduce angular dependence related to the chiral angle of the CNT in question.

2.3.2. Excited State Properties

Now, moving from ground state to excited state properties. When $\omega_i = \omega_j$ in Eq. 2.1, the energies are simply modified by J,

$$E_{\pm} = \omega \pm J. \tag{2.4}$$

For same configuration defect pairs (i.e., $ij = 11, 22, 33$) whose single-defect, or "monomer", transition energies are identical, this simplification holds and can be seen in Fig. 2.5 for 11 configurations. For increased defect separation distance, moving from axial L to 3L, the coupling between the states, J, decreases. We expect rapid decay of wavefunction overlap for 11 with increasing axial distance, as this configuration's exciton is the most localized in the single-defect regime [13, 51].

Further verifying the exciton model for J-aggregates, we see in Fig. 2.5 that the lower-energy transition state claims the oscillator strength of the higher, leaving the higher state dark. The bright state should be $\sqrt{2}$ larger than the single-defect oscillator strength [66, 67, 69, 70]. Since these systems are not ideal, the exact scaling of the oscillators is not recovered and not the purpose of our exploration and could be studied in future work. We expect to see both transitions to be nearly degenerate as defect-defect separation distance increases. Configurations 22 and 33 excitons require more separation than computational resources allow to see ideal J-type splitting as in the 11 case due to their more delocalized excitonic states (See Fig. A.4 and Fig. A.5 for 22 and 33, respectively).

Further analysis of the two coupled transitions in each panel of Fig. 2.5, now for all axial geometries, are shown in Fig. 2.6, where the interaction strengths J between the two defects were calculated by Eq. 2.2 for dissimilar defects (i.e., 21, 31, 32) and Eq. 2.4 for like-defects (i.e., 11, 22, 33). In each geometry, the two states were always chosen by the lowest bright state and the state above. Fig. 2.6(a) shows that the coupling between the defects decreases with increasing distance, which, ideally, should go like $J \sim \frac{1}{r^3}$ but due to many non-ideal conditions stemming from higher-order electrostatic interactions, wavefunction overlap, and finite CNT length, we do not reproduce this relation; to gauge this deviation, a fit to AX^n was used to quantitatively compare the results, where the power n is shown for each curve except for the highly deviating 33 defect combination.

The coupling J in the 11 case is much stronger than that for the 22 and 33 cases, as the amount of wavefunction overlap is drastically reduced moving from 22 or 33 to the 11 case. An increase in overlap leads to more complex effects that contribute to a decrease in coupling J through processes such as vibronic coupling that are not included in our model. For the off-diagonal combinations shown in Fig. 2.6(b), one can rationalize the trend in coupling through the interaction of potential wells via the amount of modulation from the pristine electronic structure shown by Table 1. The interaction of 31 (orange) will be the most coupled through electrostatics, as the type 1 defect will "cannibalize" the density from the type 3 defect due to the increased well depth of the type 1 defect. Another way to state this is that a type 3 defect does not largely change the electronic structure from the pristine case. This causes the electron density between states to largely interact, as the density-density separation becomes small. Similarly, the 21 interaction will be moderately coupled since the well depth of a type 2 defect is lower than a type 3, which implies

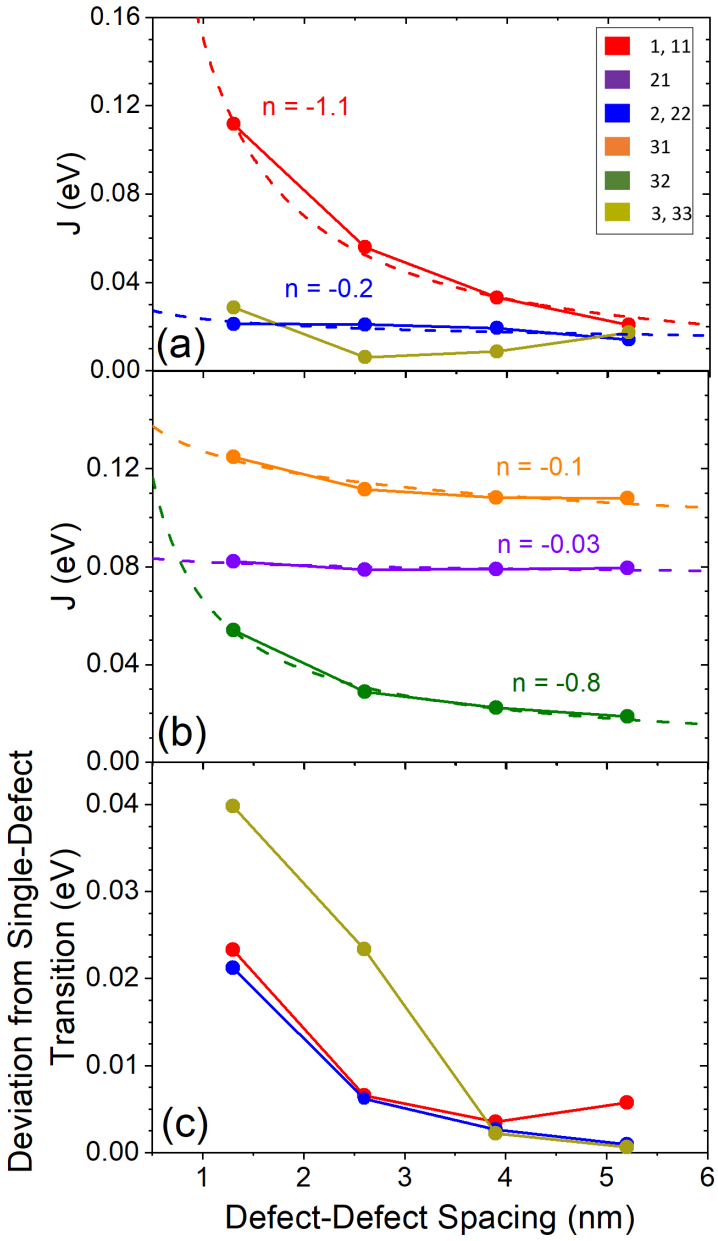

Figure 2.6. (a) J-coupling values for same-defect axial geometries (i.e. 11, 22, 33) using Eq. 2.4. (b) J-coupling values for off-diagonal defect axial geometries (i.e. 21, 31, 32) using Eq. 2.2. Dotted lines show power law fits to the data according to (Eq. 2.5), with the power from fitting is shown next to each respective line; AX^n. (c) Deviation from single-defect transition energy of the mean transition energies for same-defect axial geometries. (d) Deviation from single-defect transition energy for each defect in a pair of defects. As the defects approach infinite separation length, each panel should tend to zero for completely independent defects. Panels (a-c) conform to panel (a) legend. Panel (d) conforms to both panel (a) and (d) legends. Note the change in vertical scale of panel (d).

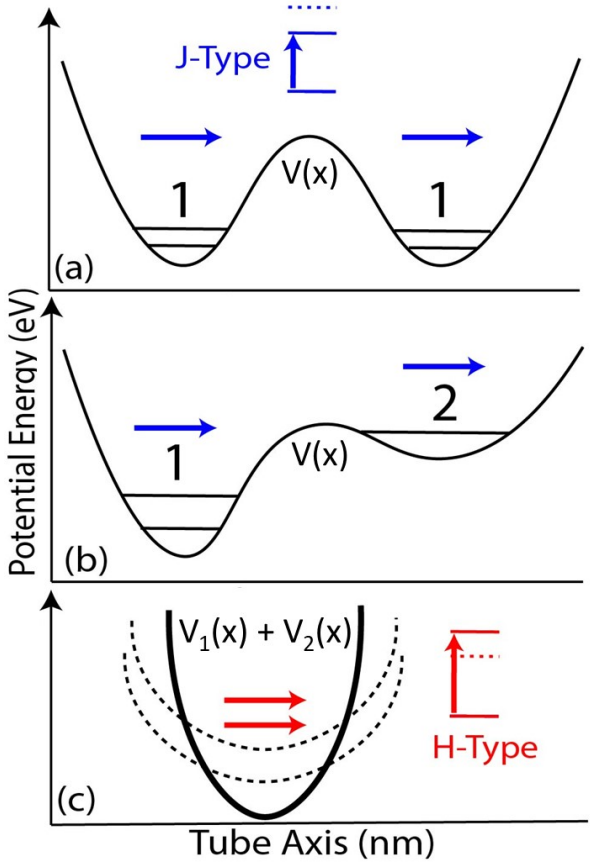

Figure 2.7. (a) Cartoon of interacting defects along the axial direction, where the transition dipole moments make a J-type aggregate. (b) Similarly to (a), the depth of the well is depicted by the intense exciton localization nature of the 1-type defect in comparison to the 2-type defect, where the 1-type "cannibalizes" the localization of the exciton. (c) Depiction of the circumferential geometry potential energy, effectively forming an H-type aggregate by the stacking of the transition dipole moments.

that some density will be retained in the type 2 well. And lastly, the 32 interaction will be the least coupled, since the type 3 and 2 defects are both delocalized and hence have shallow effective wells. The full spectra for these systems can be found in Figs. A.6, A.7, A.8, and A.9.

A number of plausible scenarios involving exciton formation, relaxation, and emission in a two-defect system warrants investigation. One way to describe these defects is to model them as one-dimensional potential wells that interact with free excitons. Fig. 2.7(a) depicts two defects of type 1 (the most red-shifted configuration), where each one maintains the same well depth and, therefore, exciton localization. Fig. 2.7(b) depicts two different defects of types 1 and 2. Type 2 has a shallower well, allowing for slightly weaker localization and more opportunity for the exciton to

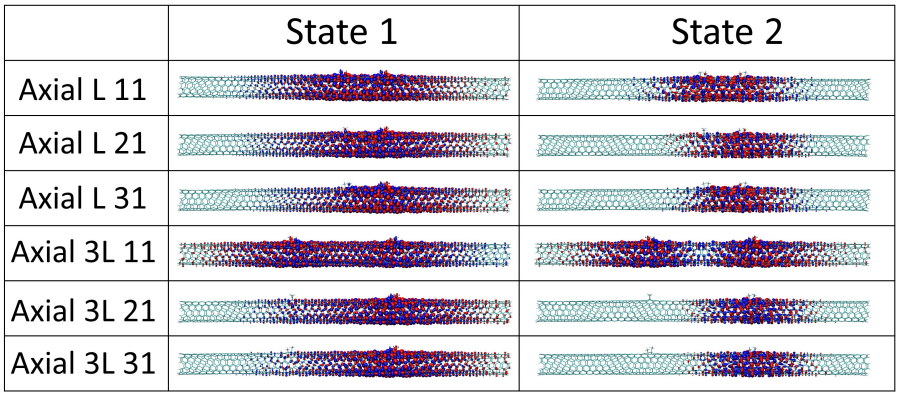

Figure 2.8. Spatially-resolved transition density for six different geometries: Axial L 11, 21, 31 and Axial 3L 11, 21, 31 showcasing the various interaction of defects from the perspective of interacting wells. The more red-shifted defects "cannibalize" the nearby density of other defects.

fall into the deeper, type 1 well. Finally, Fig. 2.7(c) shows the circumferential translation in which the wells may overlap, potentially creating a deeper well than that formed from axial translations.

Unlike molecular chromophores, for which Kasha's exciton model was originally described, CNTs connect each "monomer" through long-range conjugation, making any "through-bond" interaction between defects very important. To explore the extent to which the conjugated connections between defects is modifying the transition energy splitting from the ideal case in Eq. 2.2, we attempt to quantify the deviations present in the data of Fig 2.6(a) by defining a metric that will aid in the understanding of how non-ideal these couplings may be.

Fig. 2.6c shows the deviation of the mean transition energy between the bright and dark coupled states from the single-defect transition energy for like-defects as a function of distance r,

$$A_{ii} = \left| \frac{E_+ + E_-}{2} - \omega_i \right|. \tag{2.5}$$

where ΔJ_i the theoretical shift from the monomer transition energy of defect i and E_i is the TD-DFT defect-associated transition energy. In the infinite limit, we would expect to see two, separate transitions, one for each defect pair. Note that the type-3 defect is drastically different from its single-defect transition. This is a direct result of this configuration's delocalized nature. At energies of less than $k_BT \sim 25$ meV, recall that finite-size effects will play a larger role in resolving each data point, especially at the largest separation distance (Axial 4L), which accounts for the slight increase of less than 5 meV in some geometries moving from Axial 3L to Axial 4L in Fig. 2.6.

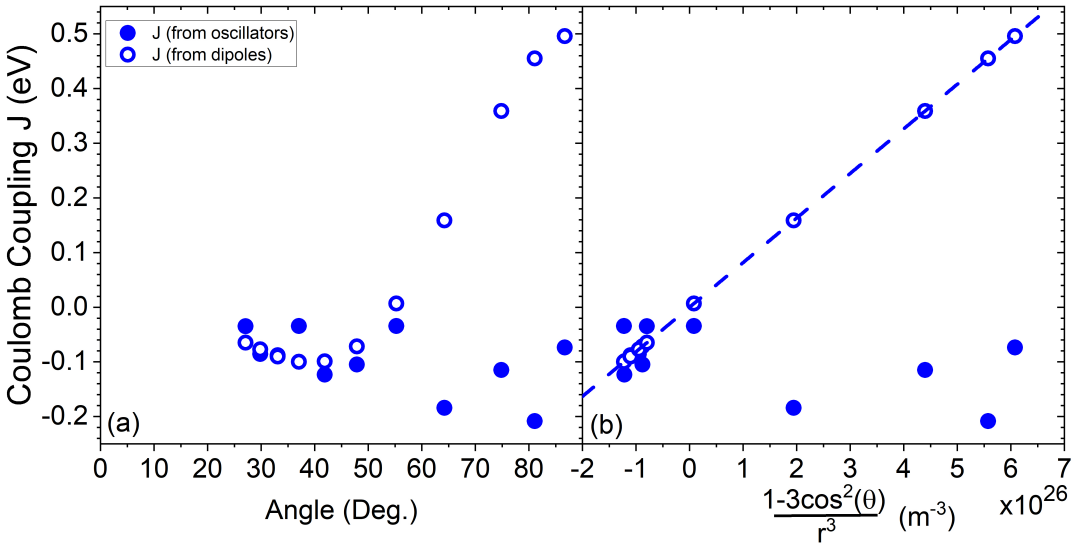

Figure 2.9. Analogously to Fig. A.11, coupling values for each method of calculation: (I) from oscillator energy splitting and (II) from single-molecule dipoles. For J-type aggregates, we see qualitative agreement between the methods, but the H-type aggregates breakdown in this comparison, as the systems never produce H-type splitting. All defects were of 11 type.

Fig. 2.8 shows transition densities for a subgroup of the axial configurations at lengths L and 3L. Different configurations have different effects on exciton trapping. The exciton interacts with the defect as a potential well and may become trapped within a single well or be shared across wells. For largely separated, identical defects such as the axial 3L 11 case, only slight excitonic density is seen near the midpoint of the defects (as in the case of state 2). For largely separated, non-identical defects, the density, for both states, is attracted to the defect with the lowest energy well. At larger separations, the transition density should decouple from the well depth, but this is not seen in these short defect-defect separation distances and is computationally infeasible to achieve such long distances.

In addition to the distance dependence of defect-defect coupling, we explore its angular dependence. We introduce a model system (see Fig. A.10), comprised of a single molecule (perylene) with a spectrally unique transition. We explore the angular dependence of the Coulomb coupling in Fig. A.11 and transition densities in Fig. A.12. See supplemental for discussion of these analyses.

In Fig. 2.9(a), we show, similarly to Fig. A.11, the coupling J as a function of interaction angle θ, which were computed using geometries (all of type 11) where a defect was first rotated circumferentially by 180° and then sequentially translated, axially, to modify the angle between

the transition dipoles and the center-to-center connecting vector between the defects. Geometries for angles θ less than 25° are not computationally feasible in this scheme for axially translated defects, as the tube would need to be longer to compensate for finite size effects [77]. The results (filled, blue circles) are qualitatively capturing the shape of the theoretical data (open, blue circles), calculated from Eq. 2.3 using single-defect dipoles; however, near the boundary to H-aggregates at roughly 60°, we see a large deviation from the theory. In fact, H-aggregates are never produced in our calculations on CNTs. Upon reaching $= 60°$, the axial separation becomes less than 1 nm, and the exciton states become highly overlapping, even for the type 1 defects. These coupled defects can now be thought of as a new type of defect; the two defects comprising this new defect lose their identities. Fig. A.13 and Fig. A.14 show spectra for geometries of angles roughly $\theta = 90°$ and $\theta = 45°$, respectively.

We now consider the fine structure of the transition densities for each geometry to explain the deviations with decreased axial separation. In Figs. A.15 and A.16 we show both transitions from six geometries with increasing axial separation. In addition, both sides of the CNT are shown for clarity. For small axial separation in the bright state (state 1), there exists an "ordered" side (A) and a "disordered" side (B). After roughly 8 Å, both sides become "ordered", which is roughly when the theoretical transition from H-type to J-type occurs at $\theta = 54°$. For the second transition state, which is dark in all cases, both sides exhibit "ordered" structure for all distances, implying that this state is largely unaffected by the relative defect locations, which is evident in their energies. The variation $(E_{MAX} - E_{MIN})$ in energy for (bright) state 1 is 0.52 eV and 0.18 eV for (dark) state 2 as shown by Fig. A.17. This shows that the bright state is strongly affected by the positioning of the defects, and this also implies that the basis functions (single-particle states) comprising these transitions are largely varying in contribution between excitonic states. The ordering and disordering of the transition densities showcases that the π-orbital conjugation is not identical on each side and possibly even broken on one side for short axial separations. The larger the separation, the easier it is to retain the conjugation through various paths, which leads to higher ordering in the transition densities, recovering generic π-π^* transition density as seen in pristine CNTs and largely single-defected CNTs.

The final comparison of the CNT system to the model through the transition densities is the symmetry of each defect. One can examine the transition density on each defect and note that the

symmetry between the defects in the lower-energy state always corresponds to the J-type aggregate, even for geometries that should be H-type aggregates according to the interaction angle argument. We have clarified some reasons for why this is the case for these CNT systems in earlier discussion. Furthermore, in all cases except one, we see the correct symmetries in the higher-energy states that would correspond to the J-type aggregate, but here we note that one of the higher-energy states exhibits varying electron-hole distributions not corresponding to the previously stated symmetry rules for the bright and dark excitons. For example, in Table S2 for axial separation of 5.7 Å, we see that all functional groups exhibit hole density; whereas, we should see that the distribution on each defect's functional groups should look like either electron-hole-hole-electron or hole-electron-electron-hole, similarly to all other axial separations shown.

2.4. Conclusions

Using TD-DFT, we have explored the interaction between spatially localized SP3-hybridization defects and showed their interaction conforms to the well-known HJ-aggregate theory (Kasha Exciton Model) describing interacting molecules in the point-dipole approximation. This is a profound result, as recent interest in CNTs for their single-photon emission in telecommunications wavelengths has prompted interest in further tunability in these emission energies through surface functionalization. Many previous studies have been done on single-defect systems, but little work has been published in multiple defects. with this knowledge of how defects may interact in the first approximation, we can apply this information to open experimental questions, such as exciton trapping energies, interacting photon emitters (i.e., second-order photon correlation and photon anti-bunching experiments) [6, 10, 81]. We clearly see that placing defects near to one another can further redshift the lowest-energy emissive state in comparison to single-defect capabilities. Although the agreement between TD-DFT calculations and Kasha's theory is not perfect, we see clear trends with interacting defects in the CNT case that can inform new experiments and further aid in the tunability of these emission energies.

We have noted that placing sets of SP3 defects, the -orbital conjugation plays an important role in tuning optical effects and can be examined through visualizing the transition density. We see that some of the circumferential geometries exhibit lower ground state energy than others. The thermodynamic and kinetic stability of these systems is of great importance to understand, as modeling with higher-accuracy methods will need to be completed on a reduced number of geome-

tries due to computational cost. However, we have briefly examined the long-range interactions of SP3-hybridization defects in a variety of configurations, but we have raised yet more quantitative questions about how defect-defect spacing affects the coupling at larger-distances-than-possible to model for this large number of geometries. In addition, we need to further flesh out how circumferentially translated defects tune the emissive-state characteristics.

REFERENCES

[1] Zixian Li, Andre Luis Branco de Barros, Daniel Cristian Ferreira Soares, Sara Nicole Moss, and Laleh Alisaraie. Functionalized single-walled carbon nanotubes: cellular uptake, biodistribution and applications in drug delivery. *International Journal of Pharmaceutics*, 524(1-2):41–54, May 2017.

[2] Yuan Cheng and Otto Zhou. Electron field emission from carbon nanotubes. *Comptes Rendus Physique*, 4(9):1021–1033, November 2003.

[3] R. H. Baughman. Carbon Nanotubes–the Route Toward Applications. *Science*, 297(5582):787–792, August 2002.

[4] Avishek Saha, Brendan J. Gifford, Xiaowei He, Geyou Ao, Ming Zheng, Hiromichi Kataura, Han Htoon, Svetlana Kilina, Sergei Tretiak, and Stephen K. Doorn. Narrow-band single-photon emission through selective aryl functionalization of zigzag carbon nanotubes. *Nature Chemistry*, 10(11):1089–1095, November 2018.

[5] Xiaowei He, Kirill A. Velizhanin, George Bullard, Yusong Bai, Jean-Hubert Olivier, Nicolai F. Hartmann, Brendan J. Gifford, Svetlana Kilina, Sergei Tretiak, Han Htoon, Michael J. Therien, and Stephen K. Doorn. Solvent- and Wavelength-Dependent Photoluminescence Relaxation Dynamics of Carbon Nanotube sp3 Defect States. *ACS Nano*, 12(8):8060–8070, August 2018.

[6] Xiaowei He, Liuyang Sun, Brendan J. Gifford, Sergei Tretiak, Andrei Piryatinski, Xiaoqin Li, Han Htoon, and Stephen K. Doorn. Intrinsic limits of defect-state photoluminescence dynamics in functionalized carbon nanotubes. *Nanoscale*, 11(18):9125–9132, 2019.

[7] Amanda R. Amori, Jamie E. Rossi, Brian J. Landi, and Todd D. Krauss. Defects Enable Dark Exciton Photoluminescence in Single-Walled Carbon Nanotubes. *The Journal of Physical Chemistry C*, 122(6):3599–3607, February 2018.

[8] Shujing Wang, Marat Khafizov, Xiaomin Tu, Ming Zheng, and Todd D. Krauss. Multiple Exciton Generation in Single-Walled Carbon Nanotubes. *Nano Letters*, 10(7):2381–2386, July 2010. Publisher: American Chemical Society.

[9] Xiaojian Wu, Mijin Kim, Haoran Qu, and YuHuang Wang. Single-defect spectroscopy in the shortwave infrared. *Nature Communications*, 10(1):1–7, June 2019.

[10] Manuel Nutz, Jiaxiang Zhang, Mijin Kim, Hyejin Kwon, Xiaojian Wu, YuHuang Wang, and Alexander Högele. Photon Correlation Spectroscopy of Luminescent Quantum Defects in Carbon Nanotubes. *Nano Letters*, 19(10):7078–7084, October 2019.

[11] Hyejin Kwon, Al'ona Furmanchuk, Mijin Kim, Brendan Meany, Yong Guo, George C. Schatz, and YuHuang Wang. Molecularly Tunable Fluorescent Quantum Defects. *Journal of the American Chemical Society*, 138(21):6878–6885, June 2016.

[12] Younghee Kim, Serguei V. Goupalov, Braden M. Weight, Brendan J. Gifford, Xiaowei He, Avishek Saha, Mijin Kim, Geyou Ao, YuHuang Wang, Ming Zheng, Sergei Tretiak, Stephen K. Doorn, and Han Htoon. Hidden Fine Structure of Quantum Defects Revealed by Single Carbon Nanotube Magneto-Photoluminescence. *ACS Nano*, February 2020. Publisher: American Chemical Society.

[13] Brendan J. Gifford, Avishek Saha, Braden M. Weight, Xiaowei He, Geyou Ao, Ming Zheng, Han Htoon, Svetlana Kilina, Stephen K. Doorn, and Sergei Tretiak. Mod(n-m,3) Dependence of Defect-State Emission Bands in Aryl-Functionalized Carbon Nanotubes. *Nano Letters*, 19(12):8503–8509, December 2019. Publisher: American Chemical Society.

[14] Marco Govoni, Ivan Marri, and Stefano Ossicini. Carrier multiplication between interacting nanocrystals for fostering silicon-based photovoltaics. *Nature Photonics*, 6(10):672–679, October 2012. Number: 10 Publisher: Nature Publishing Group.

[15] Ivan Marri, Marco Govoni, and Stefano Ossicini. Red-Shifted Carrier Multiplication Energy Threshold and Exciton Recycling Mechanisms in Strongly Interacting Silicon Nanocrystals. *Journal of the American Chemical Society*, 136(38):13257–13266, September 2014. Publisher: American Chemical Society.

[16] Marco Califano, Alex Zunger, and Alberto Franceschetti. Efficient Inverse Auger Recombination at Threshold in CdSe Nanocrystals. *Nano Letters*, 4(3):525–531, March 2004. Publisher: American Chemical Society.

[17] G. Allan and C. Delerue. Role of impact ionization in multiple exciton generation in PbSe nanocrystals. *Physical Review B*, 73(20):205423, May 2006. Publisher: American Physical Society.

[18] A. Franceschetti, J. M. An, and A. Zunger. Impact Ionization Can Explain Carrier Multiplication in PbSe Quantum Dots. *Nano Letters*, 6(10):2191–2195, October 2006. Publisher: American Chemical Society.

[19] Jun-Wei Luo, Alberto Franceschetti, and Alex Zunger. Carrier Multiplication in Semiconductor Nanocrystals: Theoretical Screening of Candidate Materials Based on Band-Structure Effects. *Nano Letters*, 8(10):3174–3181, October 2008. Publisher: American Chemical Society.

[20] Guy Allan and Christophe Delerue. Fast relaxation of hot carriers by impact ionization in semiconductor nanocrystals: Role of defects. *Physical Review B*, 79(19):195324, May 2009. Publisher: American Physical Society.

[21] Eran Rabani and Roi Baer. Distribution of Multiexciton Generation Rates in CdSe and InAs Nanocrystals. *Nano Letters*, 8(12):4488–4492, December 2008. Publisher: American Chemical Society.

[22] Márton Vörös, Dario Rocca, Giulia Galli, Gergely T. Zimanyi, and Adam Gali. Increasing impact ionization rates in Si nanoparticles through surface engineering: A density functional study. *Physical Review B*, 87(15):155402, April 2013. Publisher: American Physical Society.

[23] Andrei Kryjevski, Brendan Gifford, Svetlana Kilina, and Dmitri Kilin. Theoretical predictions on efficiency of bi-exciton formation and dissociation in chiral carbon nanotubes. *The Journal of Chemical Physics*, 145(15):154112, October 2016.

[24] Andrei Kryjevski, Deyan Mihaylov, Svetlana Kilina, and Dmitri Kilin. Multiple exciton generation in chiral carbon nanotubes: Density functional theory based computation. *The Journal of Chemical Physics*, 147(15):154106, October 2017.

[25] William Humphrey, Andrew Dalke, and Klaus Schulten. VMD: Visual molecular dynamics. *Journal of Molecular Graphics*, 14(1):33–38, February 1996.

[26] Brendan J. Gifford, Svetlana Kilina, Han Htoon, Stephen K. Doorn, and Sergei Tretiak. Exciton Localization and Optical Emission in Aryl-Functionalized Carbon Nanotubes. *The Journal of Physical Chemistry C*, 122(3):1828–1838, January 2018.

[27] G. Kresse and D. Joubert. From ultrasoft pseudopotentials to the projector augmented-wave method. *Physical Review B*, 59(3):1758–1775, January 1999. Publisher: American Physical Society.

[28] G. Kresse and J. Hafner. Ab initio molecular dynamics for liquid metals. *Physical Review B*, 47(1):558–561, January 1993. Publisher: American Physical Society.

[29] G. Kresse and J. Hafner. Ab initio molecular-dynamics simulation of the liquid-metal–amorphous-semiconductor transition in germanium. *Physical Review B*, 49(20):14251–14269, May 1994. Publisher: American Physical Society.

[30] G. Kresse and J. Furthmüller. Efficiency of ab-initio total energy calculations for metals and semiconductors using a plane-wave basis set. *Computational Materials Science*, 6(1):15–50, July 1996.

[31] G. Kresse and J. Furthmüller. Efficient iterative schemes for ab initio total-energy calculations using a plane-wave basis set. *Physical Review B*, 54(16):11169–11186, October 1996. Publisher: American Physical Society.

[32] P. E. Blöchl. Projector augmented-wave method. *Physical Review B*, 50(24):17953–17979, December 1994. Publisher: American Physical Society.

[33] John P. Perdew, Kieron Burke, and Matthias Ernzerhof. Generalized Gradient Approximation Made Simple. *Physical Review Letters*, 77(18):3865–3868, October 1996. Publisher: American Physical Society.

[34] John P. Perdew, Kieron Burke, and Matthias Ernzerhof. Generalized Gradient Approximation Made Simple [Phys. Rev. Lett. 77, 3865 (1996)]. *Physical Review Letters*, 78(7):1396–1396, February 1997. Publisher: American Physical Society.

[35] David Vanderbilt. Soft self-consistent pseudopotentials in a generalized eigenvalue formalism. *Physical Review B*, 41(11):7892–7895, April 1990. Publisher: American Physical Society.

[36] Aliaksandr V. Krukau, Oleg A. Vydrov, Artur F. Izmaylov, and Gustavo E. Scuseria. Influence of the exchange screening parameter on the performance of screened hybrid functionals. *The Journal of Chemical Physics*, 125(22):224106, December 2006. Publisher: American Institute of Physics.

[37] Jochen Heyd and Gustavo E. Scuseria. Efficient hybrid density functional calculations in solids: Assessment of the Heyd–Scuseria–Ernzerhof screened Coulomb hybrid functional. *The Journal of Chemical Physics*, 121(3):1187–1192, July 2004. Publisher: American Institute of Physics.

[38] Jochen Heyd, Gustavo E. Scuseria, and Matthias Ernzerhof. Hybrid functionals based on a screened Coulomb potential. *The Journal of Chemical Physics*, 118(18):8207–8215, April 2003. Publisher: American Institute of Physics.

[39] František Karlický and Michal Otyepka. Band Gaps and Optical Spectra of Chlorographene, Fluorographene and Graphane from G0W0, GW0 and GW Calculations on Top of PBE and HSE06 Orbitals. *Journal of Chemical Theory and Computation*, 9(9):4155–4164, September 2013. Publisher: American Chemical Society.

[40] Grigory Kolesov and Yuri Dahnovsky. Chapter 5 - Quantum Correlation Effects in Electron Dynamics in Molecular Wires and Solar Cells: The Nonequilibrium Green's Function Approach. In John R. Sabin and Erkki Brändas, editors, *Advances in Quantum Chemistry*, volume 61, pages 261–315. Academic Press, January 2011.

[41] L. P. Pitaevskii and E. M. Lifshitz. *Physical Kinetics*. Butterworth-Heinemann, December 2012. Google-Books-ID: DTHxPDfV0fQC.

[42] Andrei Kryjevski, Deyan Mihaylov, and Dmitri Kilin. Dynamics of Charge Transfer and Multiple Exciton Generation in the Doped Silicon Quantum Dot–Carbon Nanotube System: Density Functional Theory-Based Computation. *The Journal of Physical Chemistry Letters*, 9(19):5759–5764, October 2018.

[43] Lorin X. Benedict, Aaron Puzder, Andrew J. Williamson, Jeffrey C. Grossman, Giulia Galli, John E. Klepeis, Jean-Yves Raty, and O. Pankratov. Calculation of optical absorption spectra of hydrogenated Si clusters: Bethe-Salpeter equation versus time-dependent local-density

approximation. *Physical Review B*, 68(8):085310, August 2003. Publisher: American Physical Society.

[44] R. Bruce Weisman and Sergei M. Bachilo. Dependence of Optical Transition Energies on Structure for Single-Walled Carbon Nanotubes in Aqueous Suspension: An Empirical Kataura Plot. *Nano Letters*, 3(9):1235–1238, September 2003.

[45] Takumi Endo, Junko Ishi-Hayase, and Hideyuki Maki. Photon antibunching in single-walled carbon nanotubes at telecommunication wavelengths and room temperature. *Applied Physics Letters*, 106(11):113106, March 2015.

[46] X. He, H. Htoon, S. K. Doorn, W. H. P. Pernice, F. Pyatkov, R. Krupke, A. Jeantet, Y. Chassagneux, and C. Voisin. Carbon nanotubes as emerging quantum-light sources. *Nature Materials*, 17(8):663–670, August 2018.

[47] Xuedan Ma, Nicolai F. Hartmann, Jon K. S. Baldwin, Stephen K. Doorn, and Han Htoon. Room-temperature single-photon generation from solitary dopants of carbon nanotubes. *Nature Nanotechnology*, 10(8):671–675, August 2015.

[48] Svetlana Kilina, Jessica Ramirez, and Sergei Tretiak. Brightening of the Lowest Exciton in Carbon Nanotubes via Chemical Functionalization. *Nano Letters*, 12(5):2306–2312, May 2012.

[49] Svetlana Kilina, Ekaterina Badaeva, Andrei Piryatinski, Sergei Tretiak, Avadh Saxena, and Alan R. Bishop. Bright and dark excitons in semiconductor carbon nanotubes: insights from electronic structure calculations. *Physical Chemistry Chemical Physics*, 11(21):4113–4123, May 2009. Publisher: The Royal Society of Chemistry.

[50] Liujiang Zhou, Claudine Katan, Wanyi Nie, Hsinhan Tsai, Laurent Pedesseau, Jared J. Crochet, Jacky Even, Aditya D. Mohite, Sergei Tretiak, and Amanda J. Neukirch. Cation Alloying Delocalizes Polarons in Lead Halide Perovskites. *The Journal of Physical Chemistry Letters*, 10(13):3516–3524, July 2019.

[51] Brendan J. Gifford, Xiaowei He, Mijin Kim, Hyejin Kwon, Avishek Saha, Andrew E. Sifain, YuHuang Wang, Han Htoon, Svetlana Kilina, Stephen K. Doorn, and Sergei Tretiak. Op-

tical Effects of Divalent Functionalization of Carbon Nanotubes. *Chemistry of Materials*, 31(17):6950–6961, September 2019.

[52] Brendan J. Gifford, Andrew E. Sifain, Han Htoon, Stephen K. Doorn, Svetlana Kilina, and Sergei Tretiak. Correction Scheme for Comparison of Computed and Experimental Optical Transition Energies in Functionalized Single-Walled Carbon Nanotubes. *The Journal of Physical Chemistry Letters*, 9(10):2460–2468, May 2018.

[53] Sergei Tretiak, Svetlana Kilina, Andrei Piryatinski, Avadh Saxena, Richard L. Martin, and Alan R. Bishop. Excitons and Peierls Distortion in Conjugated Carbon Nanotubes. *Nano Letters*, 7(1):86–92, January 2007.

[54] Rodrigo B. Capaz, Catalin D. Spataru, Sohrab Ismail-Beigi, and Steven G. Louie. Diameter and chirality dependence of exciton properties in carbon nanotubes. *Physical Review B*, 74(12):121401, September 2006.

[55] Xiaowei He, Brendan J. Gifford, Nicolai F. Hartmann, Rachelle Ihly, Xuedan Ma, Svetlana V. Kilina, Yue Luo, Kamran Shayan, Stefan Strauf, Jeffrey L. Blackburn, Sergei Tretiak, Stephen K. Doorn, and Han Htoon. Low-Temperature Single Carbon Nanotube Spectroscopy of sp ^{3} Quantum Defects. *ACS Nano*, 11(11):10785–10796, November 2017.

[56] Yu Zheng, Sergei M. Bachilo, and R. Bruce Weisman. Controlled Patterning of Carbon Nanotube Energy Levels by Covalent DNA Functionalization. *ACS Nano*, 13(7):8222–8228, July 2019.

[57] Larry Lüer, Sajjad Hoseinkhani, Dario Polli, Jared Crochet, Tobias Hertel, and Guglielmo Lanzani. Size and mobility of excitons in (6, 5) carbon nanotubes. *Nature Physics*, 5(1):54–58, January 2009.

[58] Cathy Y. Wong, Carles Curutchet, Sergei Tretiak, and Gregory D. Scholes. Ideal dipole approximation fails to predict electronic coupling and energy transfer between semiconducting single-wall carbon nanotubes. *The Journal of Chemical Physics*, 130(8):081104, February 2009.

[59] Sergei Tretiak. Triplet State Absorption in Carbon Nanotubes: A TDDFT Study. *Nano Letters*, 7(8):2201–2206, August 2007.

[60] Sergei Tretiak and Shaul Mukamel. Density Matrix Analysis and Simulation of Electronic Excitations in Conjugated and Aggregated Molecules. *Chemical Reviews*, 102(9):3171–3212, September 2002.

[61] Marc Dvorak, Su-Huai Wei, and Zhigang Wu. Origin of the Variation of Exciton Binding Energy in Semiconductors. *Physical Review Letters*, 110(1):016402, January 2013.

[62] Jan T. Glückert, Lyudmyla Adamska, Wolfgang Schinner, Matthias S. Hofmann, Stephen K. Doorn, Sergei Tretiak, and Alexander Högele. Dipolar and charged localized excitons in carbon nanotubes. *Physical Review B*, 98(19):195413, November 2018.

[63] Yuhei Miyauchi, Munechiyo Iwamura, Shinichiro Mouri, Tadashi Kawazoe, Motoichi Ohtsu, and Kazunari Matsuda. Brightening of excitons in carbon nanotubes on dimensionality modification. *Nature Photonics*, 7(9):715–719, September 2013.

[64] Vasili Perebeinos, J. Tersoff, and Phaedon Avouris. Scaling of Excitons in Carbon Nanotubes. *Physical Review Letters*, 92(25):257402, June 2004.

[65] Dominik Stich, Florian Späth, Hannes Kraus, Andreas Sperlich, Vladimir Dyakonov, and Tobias Hertel. Triplet–triplet exciton dynamics in single-walled carbon nanotubes. *Nature Photonics*, 8(2):139–144, February 2014.

[66] M. Kasha, H. R. Rawls, and M. Ashraf El-bayoumi. The exciton model in molecular spectroscopy. *Pure Appl. Chem. 1965*, pages 371–592.

[67] Michael Kasha. Energy Transfer Mechanisms and the Molecular Exciton Model for Molecular Aggregates. *Radiation Research*, 20(1):55–70, 1963.

[68] Robin M. Hochstrasser and Michael Kasha. Application of the Exciton Model to Mono-Molecular Lamellar Systems*. *Photochemistry and Photobiology*, 3(4):317–331, 1964.

[69] Nicholas J. Hestand and Frank C. Spano. Expanded Theory of H- and J-Molecular Aggregates: The Effects of Vibronic Coupling and Intermolecular Charge Transfer. *Chemical Reviews*, 118(15):7069–7163, August 2018.

[70] Nicholas J. Hestand and Frank C. Spano. Molecular Aggregate Photophysics beyond the Kasha Model: Novel Design Principles for Organic Materials. *Accounts of Chemical Research*, 50(2):341–350, February 2017.

[71] Hajime Yamagata and Frank C. Spano. Strong Photophysical Similarities between Conjugated Polymers and J-aggregates. *The Journal of Physical Chemistry Letters*, 5(3):622–632, February 2014.

[72] Gregory D. Scholes, Kenneth P. Ghiggino, Anna M. Oliver, and Michael N. Paddon-Row. Through-space and through-bond effects on exciton interactions in rigidly linked dinaphthyl molecules. *Journal of the American Chemical Society*, 115(10):4345–4349, May 1993.

[73] Robert L. Fulton and Martin Gouterman. Vibronic Coupling. II. Spectra of Dimers. *The Journal of Chemical Physics*, 41(8):2280–2286, October 1964.

[74] Andrzej Witkowski and William Moffitt. Electronic Spectra of Dimers: Derivation of the Fundamental Vibronic Equation. *The Journal of Chemical Physics*, 33(3):872–875, September 1960.

[75] Christopher M. Pochas, Kurt A. Kistler, Hajime Yamagata, Spiridoula Matsika, and Frank C. Spano. Contrasting Photophysical Properties of Star-Shaped vs Linear Perylene Diimide Complexes. *Journal of the American Chemical Society*, 135(8):3056–3066, February 2013.

[76] Y. J. Dappe, J. Ortega, and F. Flores. Intermolecular interaction in density functional theory: Application to carbon nanotubes and fullerenes. *Physical Review B*, 79(16):165409, April 2009.

[77] Anurag Sharma, Brendan J. Gifford, and Svetlana Kilina. Tip Functionalization of Finite Single-Walled Carbon Nanotubes and Its Impact on the Ground and Excited State Electronic Structure. *The Journal of Physical Chemistry C*, 121(15):8601–8612, April 2017.

[78] M. J. Frisch, G. W. Trucks, H. B. Schlegel, G. E. Scuseria, M. A. Robb, J. R. Cheeseman, G. Scalmani, V. Barone, G. A. Petersson, H. Nakatsuji, X. Li, M. Caricato, A. V. Marenich, J. Bloino, B. G. Janesko, R. Gomperts, B. Mennucci, H. P. Hratchian, J. V. Ortiz, A. F. Izmaylov, J. L. Sonnenberg, Williams, F. Ding, F. Lipparini, F. Egidi, J. Goings, B. Peng, A. Petrone, T. Henderson, D. Ranasinghe, V. G. Zakrzewski, J. Gao, N. Rega, G. Zheng,

W. Liang, M. Hada, M. Ehara, K. Toyota, R. Fukuda, J. Hasegawa, M. Ishida, T. Nakajima, Y. Honda, O. Kitao, H. Nakai, T. Vreven, K. Throssell, J. A. Montgomery Jr., J. E. Peralta, F. Ogliaro, M. J. Bearpark, J. J. Heyd, E. N. Brothers, K. N. Kudin, V. N. Staroverov, T. A. Keith, R. Kobayashi, J. Normand, K. Raghavachari, A. P. Rendell, J. C. Burant, S. S. Iyengar, J. Tomasi, M. Cossi, J. M. Millam, M. Klene, C. Adamo, R. Cammi, J. W. Ochterski, R. L. Martin, K. Morokuma, O. Farkas, J. B. Foresman, and D. J. Fox. Gaussian 16 Rev. C.01, 2016.

[79] Richard L. Martin. Natural transition orbitals. *The Journal of Chemical Physics*, 118(11):4775–4777, February 2003.

[80] Tian Lu and Feiwu Chen. Multiwfn: A multifunctional wavefunction analyzer. *Journal of Computational Chemistry*, 33(5):580–592, 2012.

[81] Younghee Kim, Kirill A. Velizhanin, Xiaowei He, Ibrahim Sarpkaya, Yohei Yomogida, Takeshi Tanaka, Hiromichi Kataura, Stephen K. Doorn, and Han Htoon. Photoluminescence Intensity Fluctuations and Temperature-Dependent Decay Dynamics of Individual Carbon Nanotube sp3 Defects. *The Journal of Physical Chemistry Letters*, 10(6):1423–1430, March 2019.

APPENDIX. SUPPLEMENTAL INFORMATION

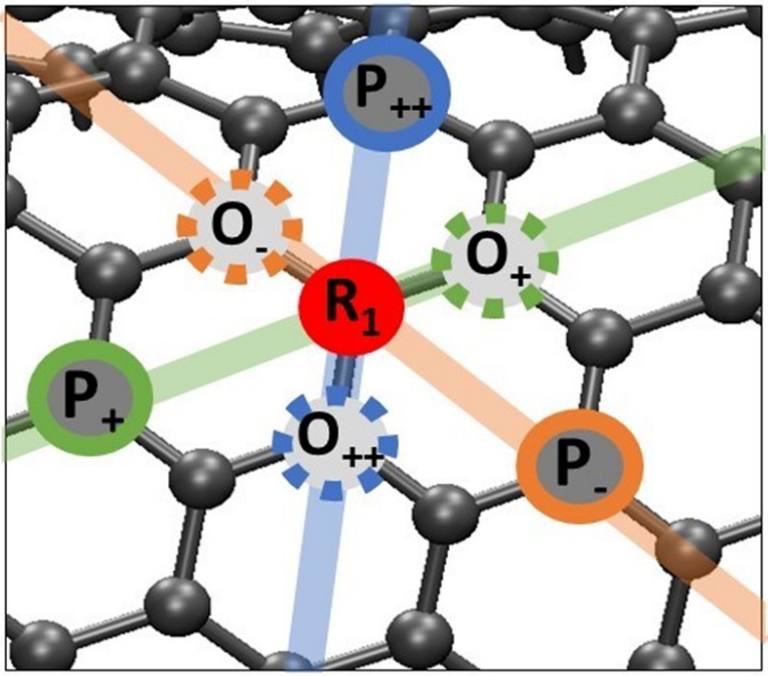

Figure A.1. Definition of defect orientation. With one attachment placed at R_1, the second attachment can be placed in any of the nearest six carbon atoms: Three ortho and three para to the original location. In this study, we restrict ourselves to the most and least redshifted configurations: P+ and O+, respectively.

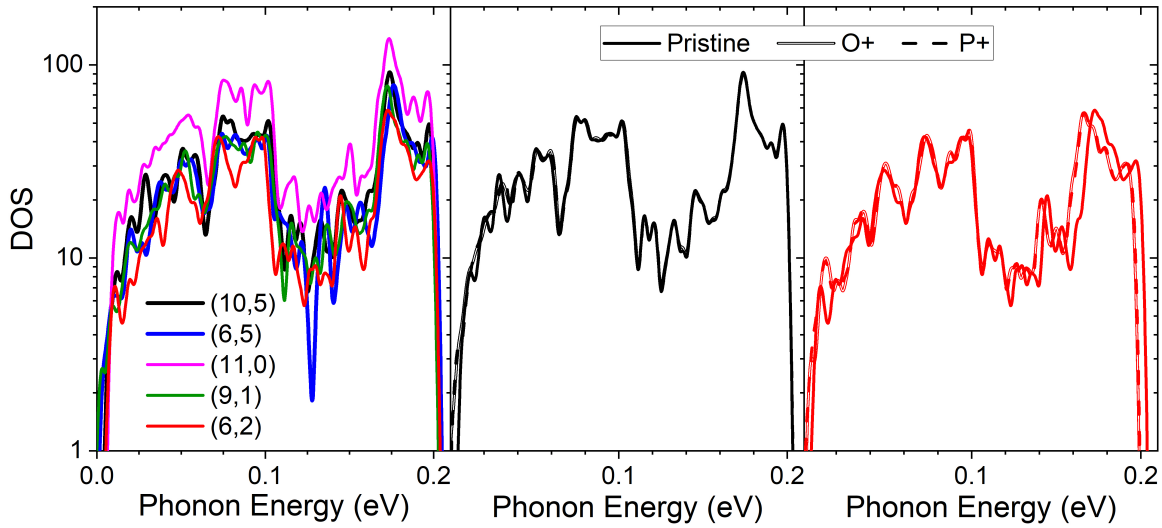

Figure A.2. Phonon density of states (DOS) for all pristine (a) and chlorine-functionalized (b,c) CNTs. Phonon spectrum was computed using VASP at the PBE level using two-point differences. Due to the more narrow (6,2) CNT, we see larger differences arising from the increased curvature as well as smaller number of defect atoms to total atoms in comparison to (10,5). Note the units of DOS are inverse energy and that thermally broadened δ-functions (Gaussian width = 25 meV) were used.

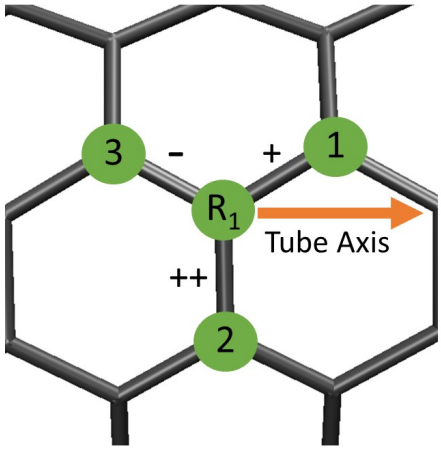

Figure A.3. Definition of defect configuration. One covalently bonded group is fixed at R1, but there are three (i.e., type 1, 2, or 3) non-equivalent ortho positions to place the second covalent attachment (needed for closed shell system). In previous works using the (6,5) CNT, these were labeled as O+, O++, and O- or as L30, L90, and L-30. Here we employ a chirality independent nomenclature to describe the defects by their amount of redshift produced from the pristine E11 band.

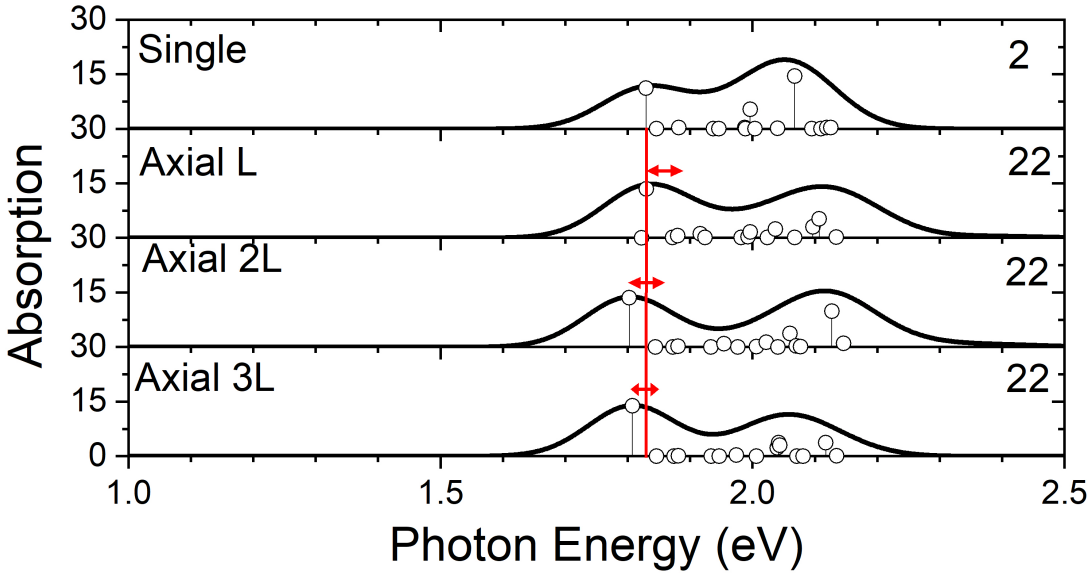

Figure A.4. Absorption spectrum for four geometries, including both the bright pristine E11 transition (∼2.05 eV) and the bright (and dark) defect-associated transitions (∼1.8 – 1.9 eV). Single defect in the 2-type configuration as reference for the J coupling value. With increasing distance L, 2L, to 3L, we see an increase in J-splitting symmetry as well as a decrease in J-splitting magnitude, except for the smallest distance "Axial L" due to intense wavefunction overlap. The midpoint of the splitting becomes more and more symmetric due to the increase in distance, which implies that the wavefunctions of each defect are becoming less overlapped and becoming more and more ideal to the simple Kasha model. In addition, since $J \sim 1/r^3$, the magnitude of splitting decreases with increasing defect-defect distance r. Note that the vertical axis scale represents unitless oscillator strength and not absorption, which has arbitrary units.

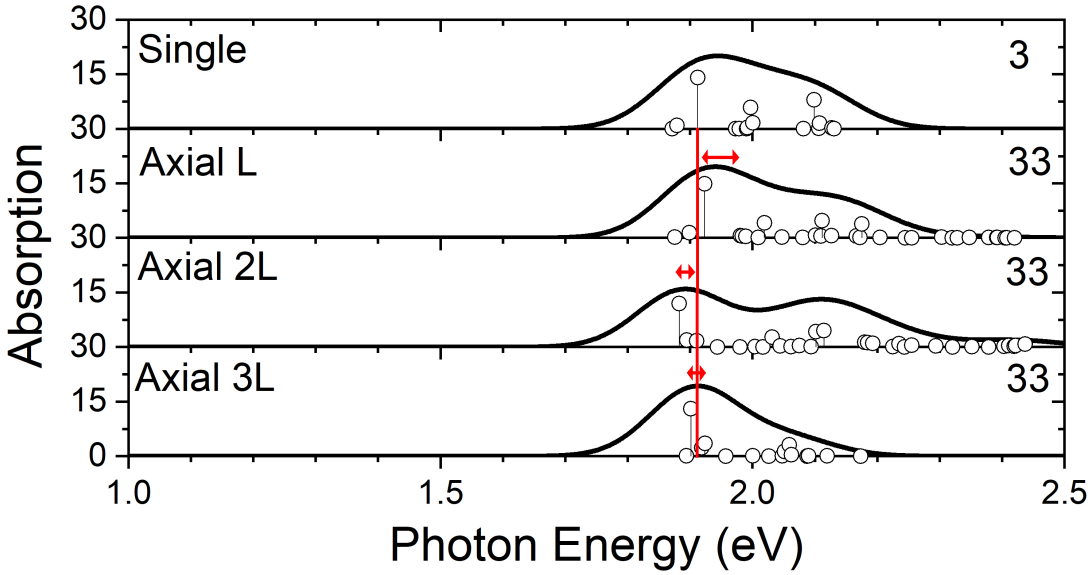

Figure A.5. S2: Absorption spectrum for four geometries, including both the bright pristine E11 transition (∼2.05 eV) and the bright (and dark) defect-associated transitions (∼1.85 – 1.95 eV). Single defect in the 3-type configuration as reference for the J coupling value. With increasing distance L, 2L, to 3L, we see an increase in J-splitting symmetry as well as a decrease in J-splitting magnitude. The midpoint of the splitting becomes more and more symmetric due to the increase in distance, which implies that the wavefunctions of each defect are becoming less overlapped and becoming more and more ideal to the simple Kasha model. In addition, since $J \sim 1/r^3$, the magnitude of splitting decreases with increasing defect-defect distance r. Note that the vertical axis scale represents unitless oscillator strength and not absorption, which has arbitrary units.

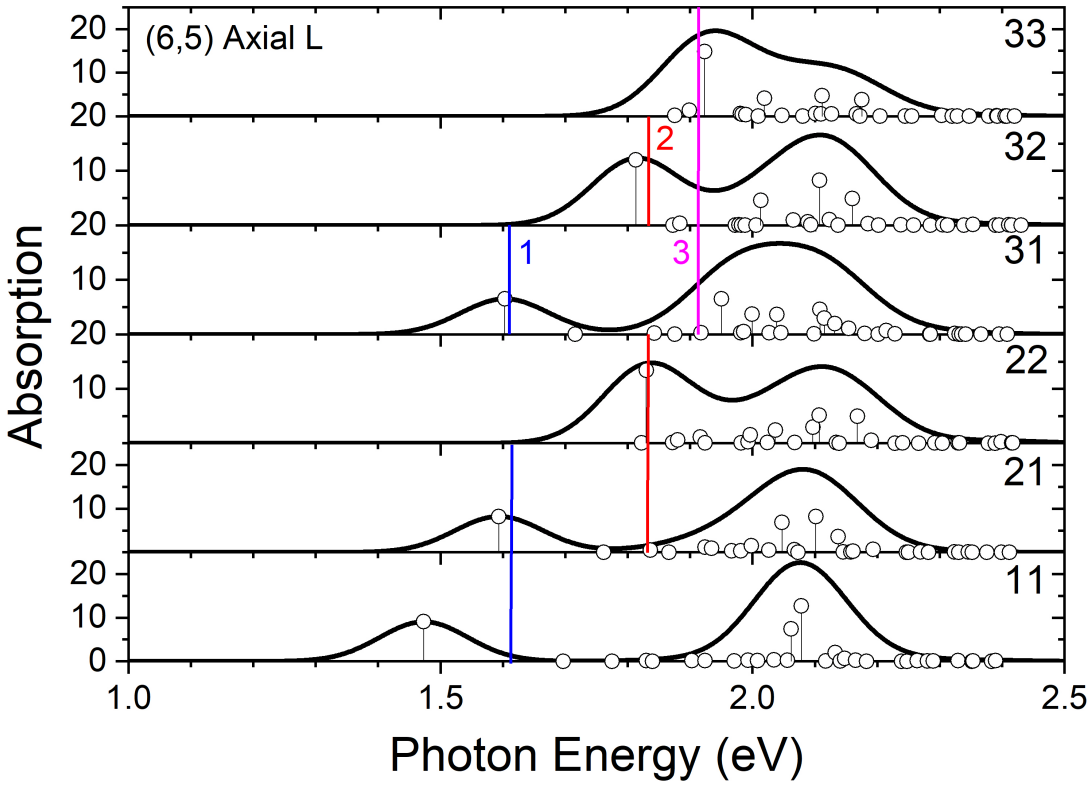

Figure A.6. Absorption spectrum for all six combinations of defect pairs with a separation distance of L. Note that the vertical axis scale represents unitless oscillator strength and not absorption, which has arbitrary units.

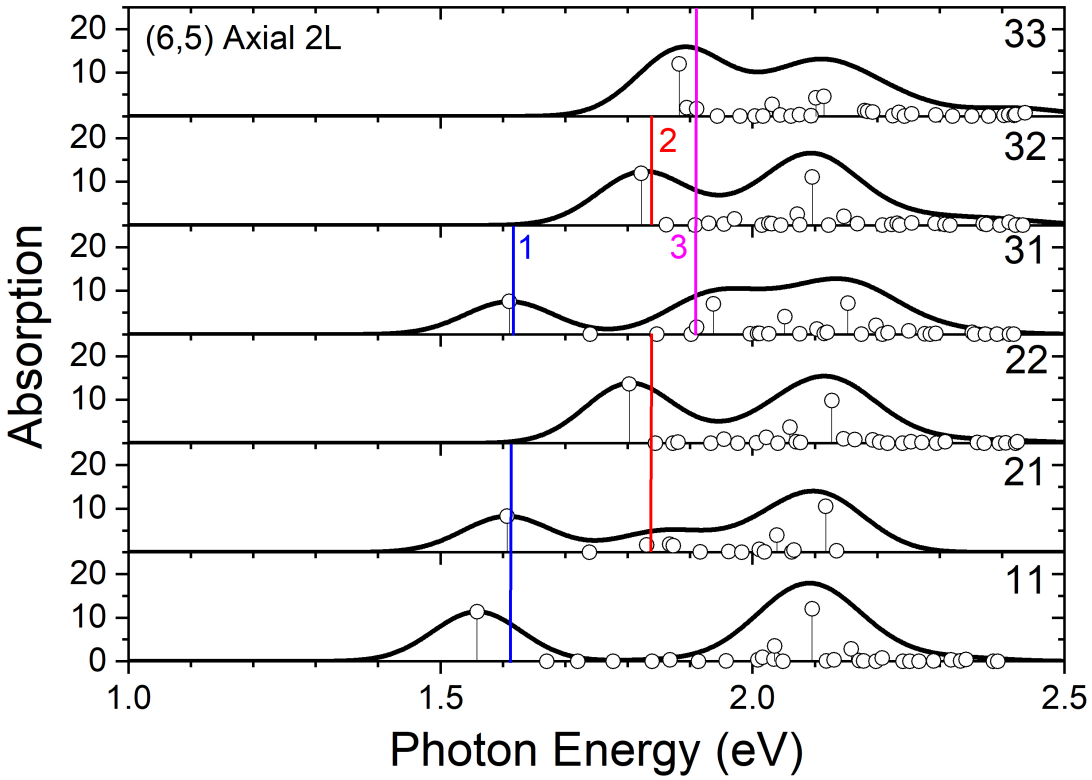

Figure A.7. Absorption spectrum for all six combinations of defect pairs with a separation distance of 2L. Note that the vertical axis scale represents unitless oscillator strength and not absorption, which has arbitrary units.

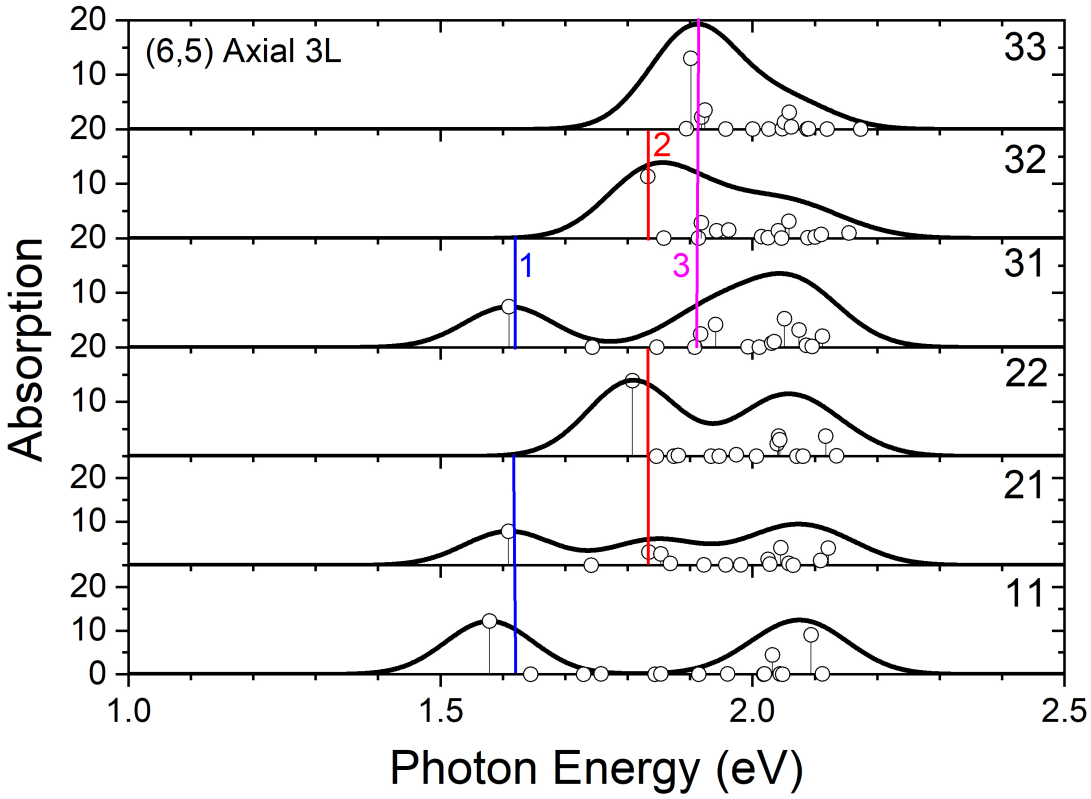

Figure A.8. Absorption spectrum for all six combinations of defect pairs with a separation distance of 3L. Note that the vertical axis scale represents unitless oscillator strength and not absorption, which has arbitrary units.

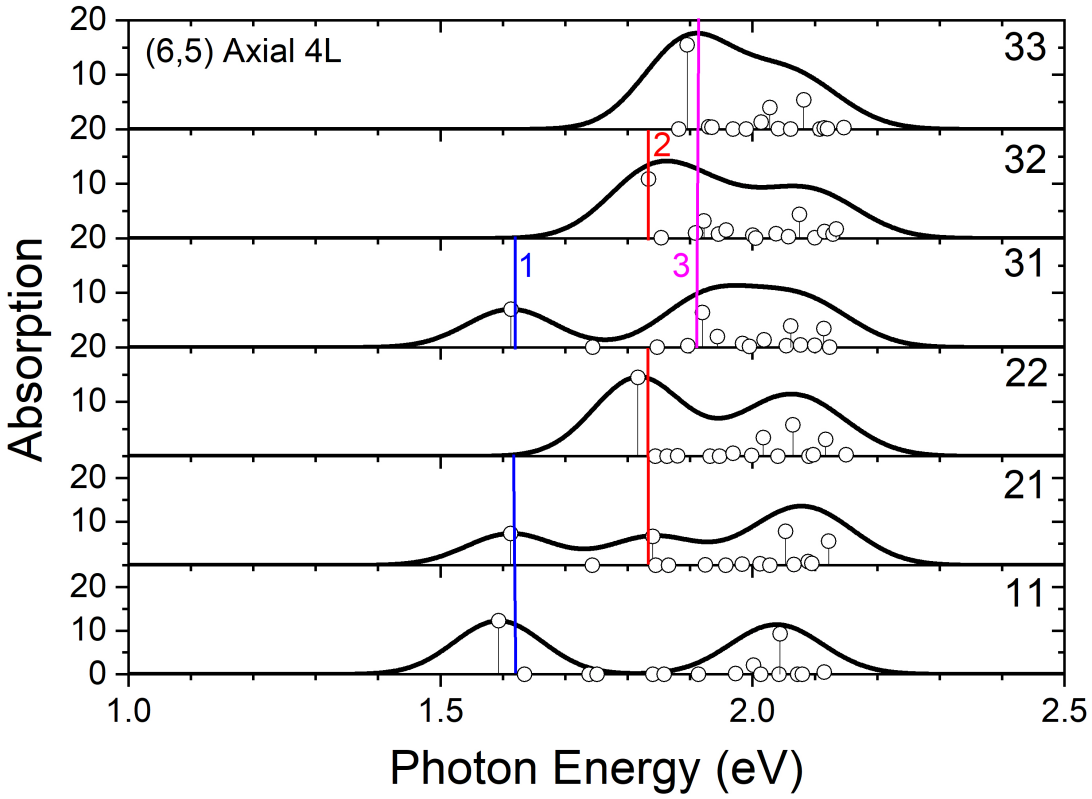

Figure A.9. Absorption spectrum for all six combinations of defect pairs with a separation distance of 4L. Note that the vertical axis scale represents unitless oscillator strength and not absorption, which has arbitrary units.

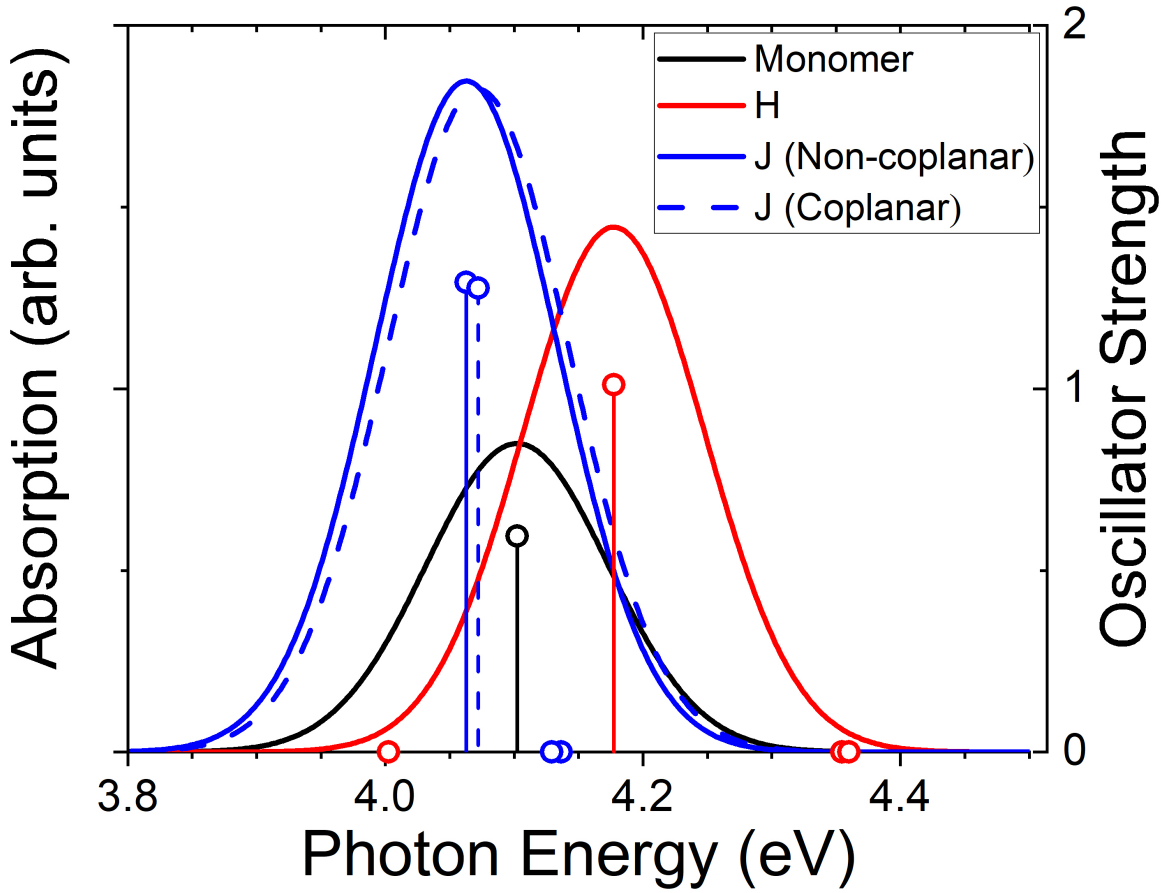

Figure A.10. Absorption spectra of the model system, comprised of interacting single molecules. Showing the monomer transition (black) for reference, we computed the H-aggregate (red) limit and the J-aggregate (blue) limit to compare the unique qualities of each for use of analysis of the more complicated CNT case. We introduce a model system (see Fig. A.10), comprised of a single molecule (perylene) with a spectrally unique transition near 4.1 eV (as calculated from TD-DFT at the same level of theory as our CNT calculations). Fig. A.10 shows the limiting cases of H- (red) and J- (blue) aggregate geometries that blue-shift and red-shift the bright state, respectively, in comparison to the monomer transition energy (black). A scan over the angle between the transition dipole and the center-to-center vector between the molecules is carried out by starting with a stacked geometry (H-aggregate, $\theta = 90°$) and shifting the bottom molecule along the slip plane.

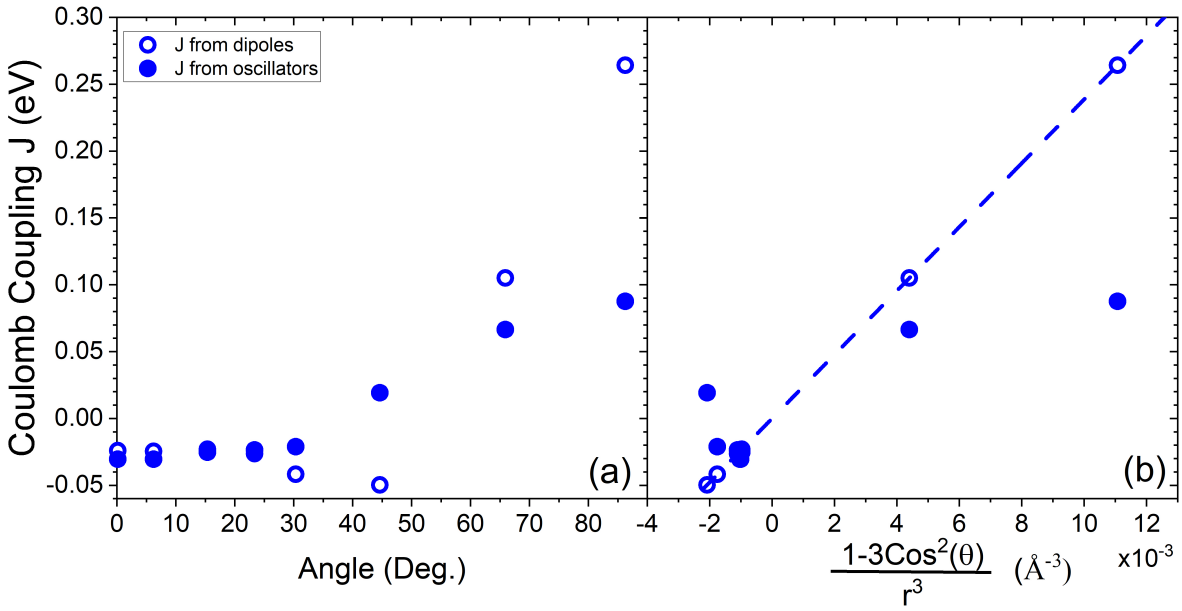

Figure A.11. Coulomb coupling values for each method of calculation: (I) from oscillator energy splitting and (II) from single-molecule dipoles, where the latter assumes the form of the coupling, but the former does not. We see qualitative agreement between the two methods, especially for J-type interaction regions. Using Eq. 2.2 and Eq. 2.3 to calculate, separately, the coupling via oscillators and single-monomer transition dipoles, we provide direct comparison between the theory and numerical experiment. Fig. S8a shows the coupling is plotted against the angle of interaction using the center of mass of each molecule as its transition dipole origin. The coupling plotted against the independent variable in the point dipole approximation. The form of this function was explicitly used to acquire the coupling from the dipoles, so this depiction expands on where the method of oscillators deviates from this model. The deviations occur around $\theta = 30°$, where we expect the point dipole approximation to become less trustworthy. To minimize the vibrational coupling in this molecular system when stacked, which has been studied in depth by various groups, a slightly larger distance than would appear in experiment was used as the stacking distance to concentrate purely on the long-range Coulomb interactions. In addition, there may be errors stemming from our limited basis and methodology that contribute to these deviations. Even though the shape of the curve is modified through these higher-order effects, the general form of the function with regards to the dipole approximation is recovered and can be used in comparison to the CNT system.

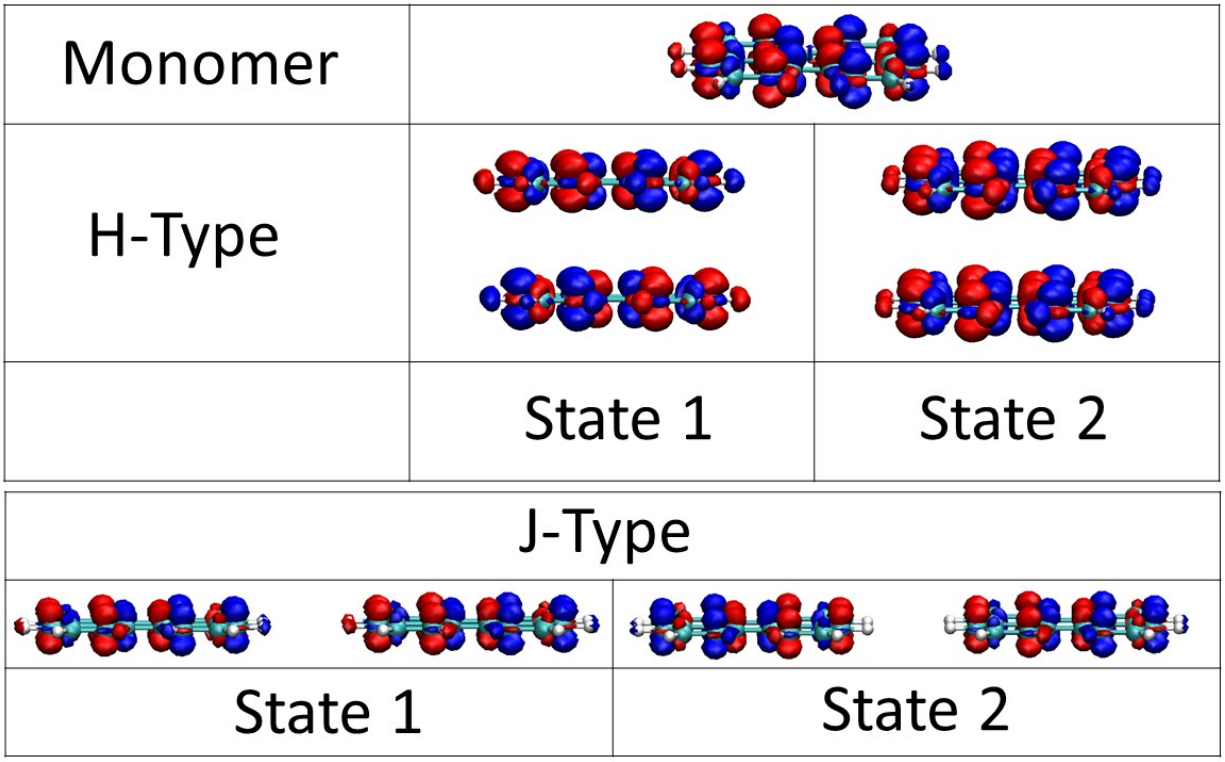

Figure A.12. Transition density is shown for the model system in three geometries, the monomer and two dimers that are the limiting cases of the interaction angle θ. We note simply the symmetries for each set of aggregates that exhibit bright transitions and dark transitions. In addition to calculating the Coulomb coupling of these interactions, we may examine these objects from a visual perspective by plotting the transition density for the two excited states in question and examining the unique qualities of each type of aggregate. In Fig. A.12, we show transition density for three systems: (I) monomer, (II) H-type aggregate, and (III) J-type aggregate. For the two aggregates, we also show the two interacting states, $S_{1,2}$, where we know from the effective exciton model, that the lower state should be dark (H-type) for one and bright (J-type) for the other. After examination of the transition density, we find that there are inherent symmetries with respect to the transition states of each molecule in the dimer that will allow or disallow that optical transition, which we will not discuss in depth, as this is already well known. We simply note that one molecule in a dimer will always resemble the single-molecule (monomer) case, and the other molecule is either identical or related to the first by a C2 rotation about the axis perpendicular to the plane of the molecule. When the dimer exhibits the latter property, the state is said to be dark, which physically manifests itself in the fact that the electric transition dipoles are now anti-parallel, since the electron and hole spatial occupations have switched. In the bright case, the transition densities of both molecules are identical to each other and, hence, have parallel dipoles.

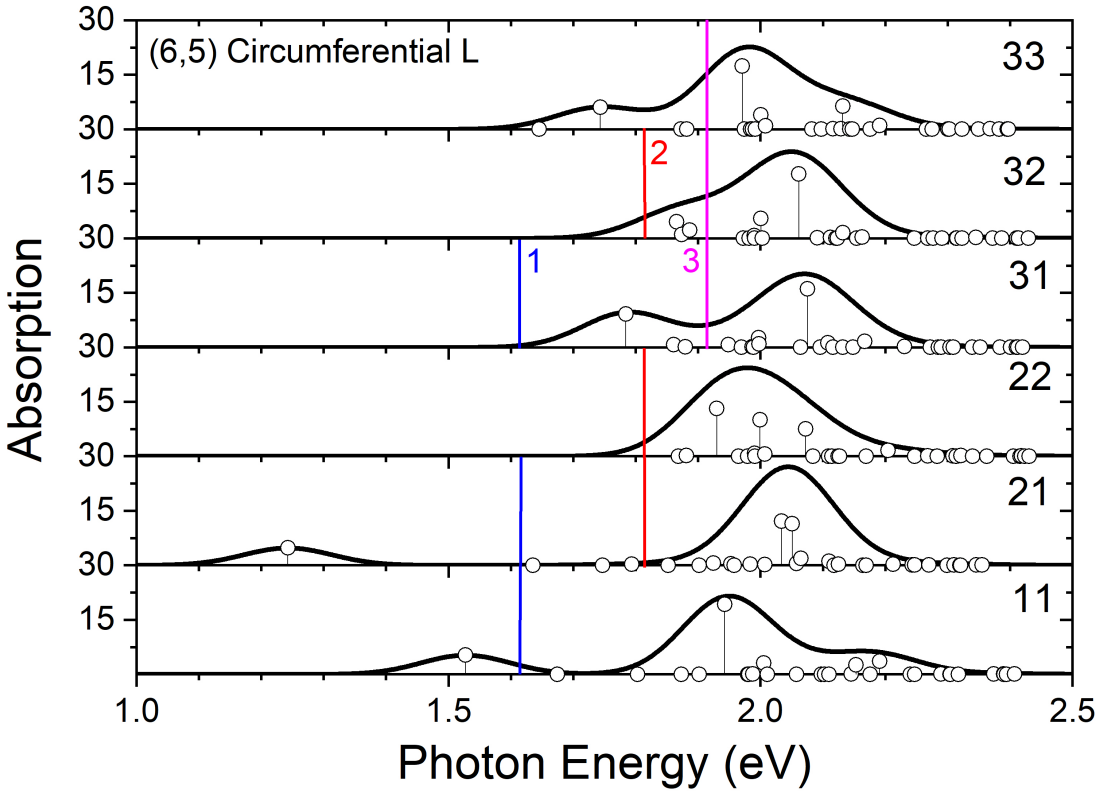

Figure A.13. Absorption spectrum for all six combinations of defect pairs with circumferential translation, $\theta \sim 90°$. Note that the vertical axis scale represents unitless oscillator strength and not absorption, which has arbitrary units.

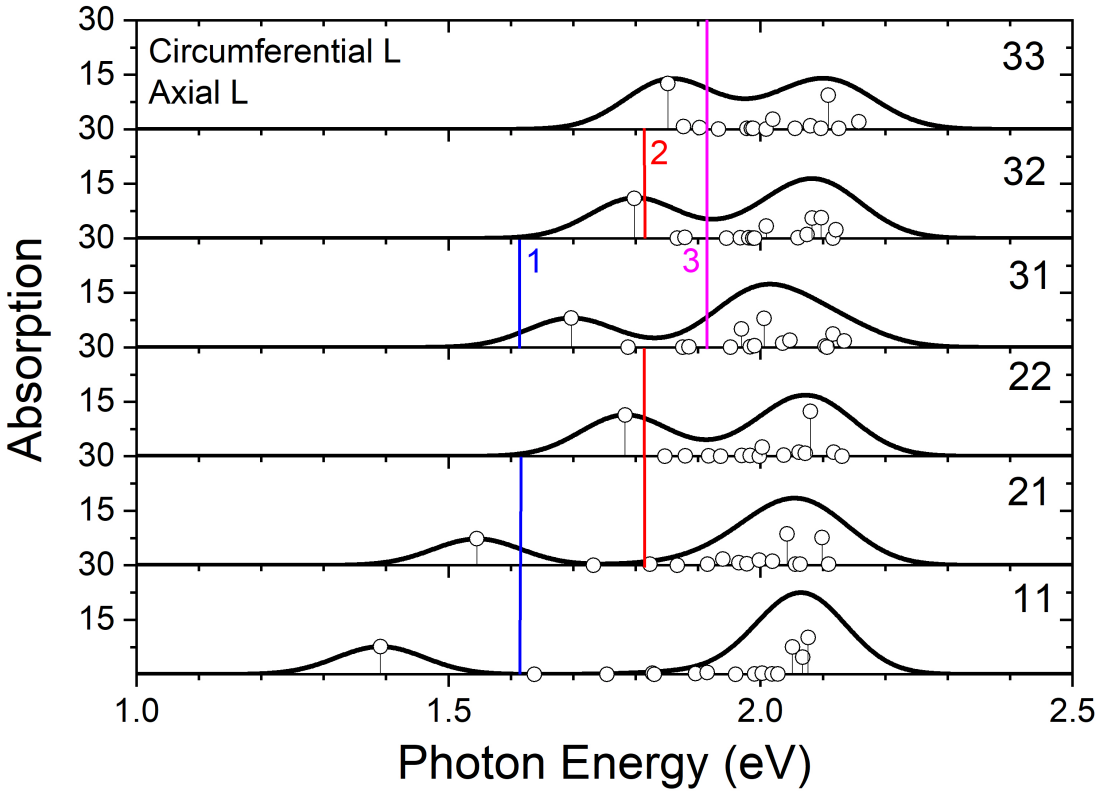

Figure A.14. Absorption spectrum for all six combinations of defect pairs with circumferential translation and axial translation such that $\theta \sim 45°$. Note that the vertical axis scale represents unitless oscillator strength and not absorption, which has arbitrary units.

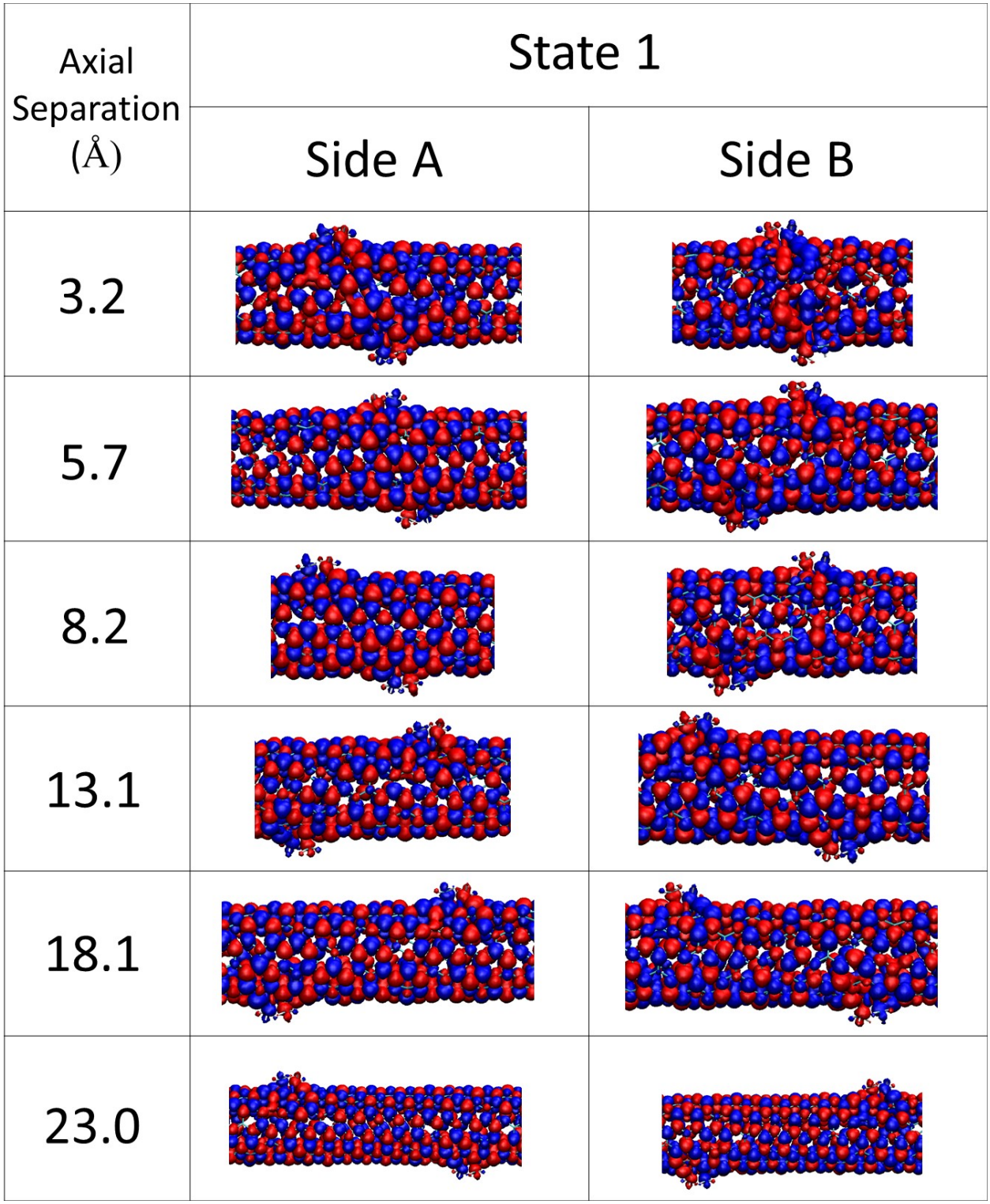

Figure A.15. Transition density for various type 11 CNT systems that have been used to sample the angle space of this interaction. One defect was circumferentially translated and then axially translated by various lengths. These densities show various important characteristics from symmetry of each defect to the ordered state along each side of the CNT.

Axial Separation (Å)	State 2	
	Side A	Side B
3.2	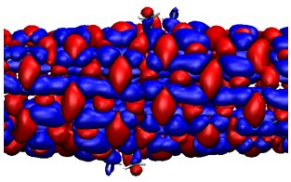	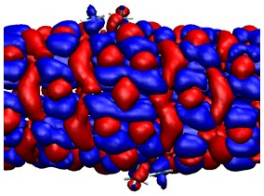
5.7	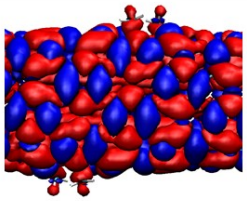	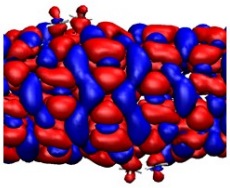
8.2	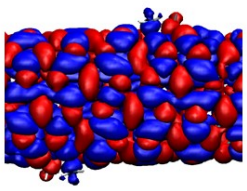	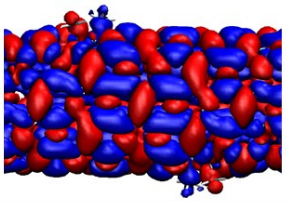
13.1	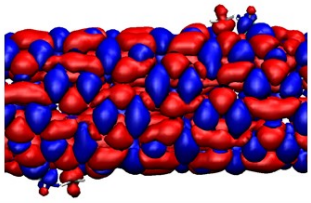	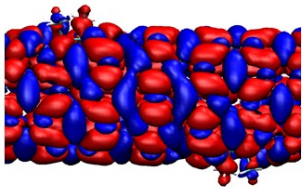
18.1	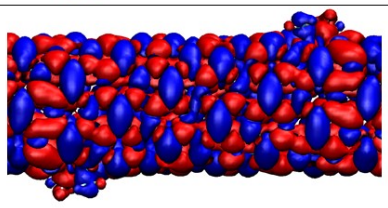	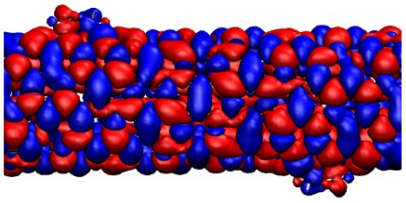
23.0	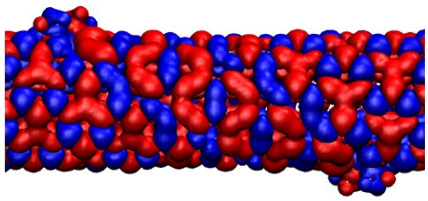	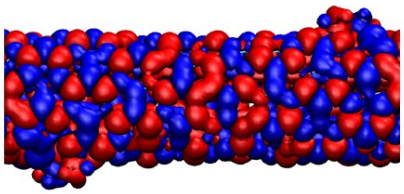

Figure A.16. Transition density for various type 11 CNT systems that have been used to sample the angle space of this interaction. One defect was circumferentially translated and then axially translated by various lengths. These densities show various important characteristics from symmetry of each defect to the ordered state along each side of the CNT.

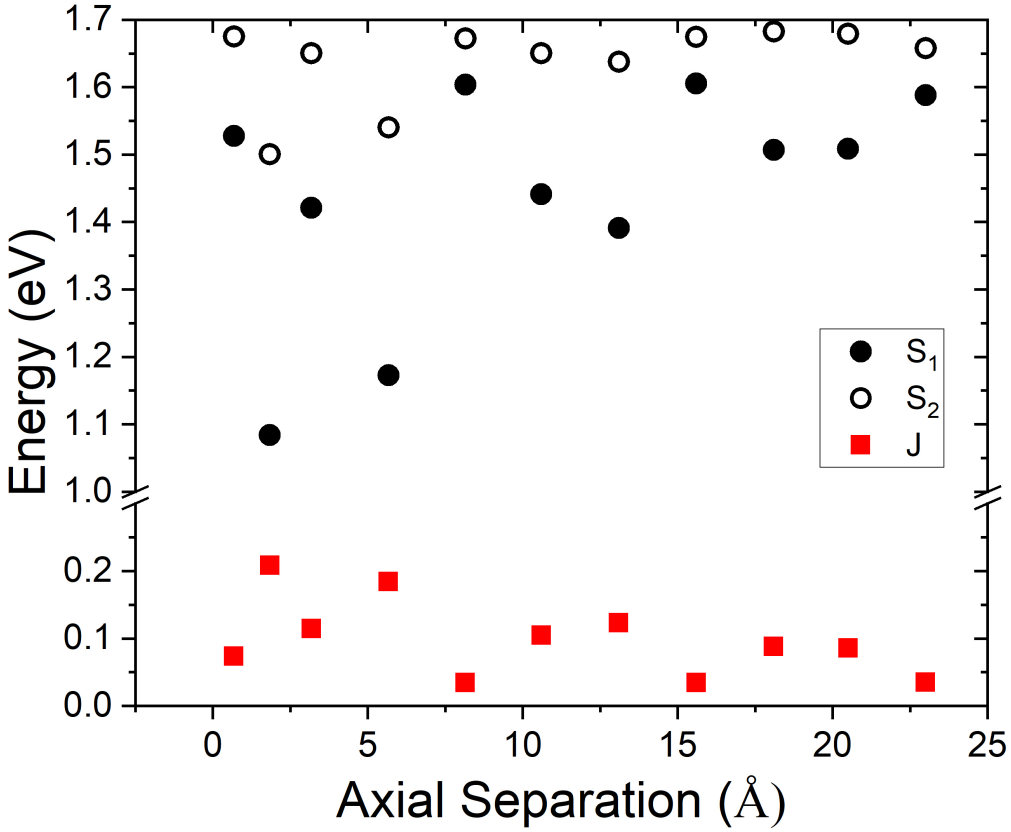

Figure A.17. Energies of CNT excited states S_1 and S_2, also plotted with the Coulomb coupling as a function of axial separation.